

# JGR Solid Earth

## RESEARCH ARTICLE

10.1029/2019JB018566

### Key Points:

- We develop a semiautomated method for estimating finite fault parameters of earthquakes with second seismic moments
- Resolved rupture directivities are generally consistent with expectations for dynamic ruptures on the imaged velocity contrasts
- Stress drops and uncertainties are estimated for elliptical ruptures using the derived characteristic rupture length and width

### Supporting Information:

- Supporting Information S1

### Correspondence to:

H. Meng,  
haoranme@usc.edu

### Citation:

Meng, H., McGuire, J. J., & Ben-Zion, Y. (2020). Semiautomated estimates of directivity and related source properties of small to moderate southern California earthquakes using second seismic moments. *Journal of Geophysical Research: Solid Earth*, 125, e2019JB018566. <https://doi.org/10.1029/2019JB018566>

Received 20 AUG 2019

Accepted 9 FEB 2020

Accepted article online 11 FEB 2020

## Semiautomated Estimates of Directivity and Related Source Properties of Small to Moderate Southern California Earthquakes Using Second Seismic Moments

Haoran Meng<sup>1,2</sup> , Jeffrey J. McGuire<sup>3</sup> , and Yehuda Ben-Zion<sup>1</sup> 

<sup>1</sup>Department of Earth Sciences, University of Southern California, Los Angeles, CA, USA, <sup>2</sup>Department of Earth, Ocean and Atmospheric Science, Florida State University, Tallahassee, FL, USA, <sup>3</sup>U.S. Geological Survey, CA, USA

**Abstract** We develop a semiautomated method for estimating with second seismic moments the directivity, rupture area, duration, and centroid velocity of earthquakes. The method is applied to 41 southern California earthquakes with magnitude in the range 3.5–5.2 and provides stable results for 28 events. Apparent source time functions (ASTFs) of *P* and *S* phases are derived using deconvolution with three stacked empirical Green's functions (seGf). The use of seGf suppresses nongeneric source effects, improves the focal mechanism correspondence to the analyzed earthquakes, and typically allows inclusion of 5 to 15 more ASTFs compared with analysis using a single eGf. Most analyzed earthquakes in the Trifurcation area of the San Jacinto Fault have directivities toward the northwest, while events around Cajon Pass and San Gabriel Mountain tend to propagate toward the southeast. These results are generally consistent with predictions for dynamic rupture on bimaterial interfaces associated with the imaged velocity contrasts in the area. The second moment inversions also provide constraints on the upper and lower bounds of rupture areas in our data set. Stress drops and uncertainties are estimated for elliptical ruptures using the derived characteristic rupture length and width. The semiautomated second moment method with seGfs can be used for routine application to moderate earthquakes in locations with good station coverage.

## 1. Introduction

Earthquake catalogs typically represent seismic events as point sources with location, time, magnitude, and focal mechanism (e.g., Hauksson et al., 2012; White et al., 2019; Yang et al., 2012). The “cut and paste” technique was developed to estimate the centroid location, time, and focal mechanism using broadband regional seismograms (e.g., Zhao & Helmberger, 1994; Zhu & Ben-Zion, 2013; Zhu & Helmberger, 1996). The centroid location and time are spatial and temporal means (first degree moment) of the earthquake moment rate function and are routinely cataloged from both regional and global seismic networks. Second-degree seismic moments (variances) of the moment rate function provide the simplest representation of source finiteness that includes rupture extent, duration and directivity (e.g. Backus, 1977a, 1977b; Backus & Mulcahy, 1976a, 1976b; McGuire, 2004; McGuire, 2017). Descriptions of source finiteness, however, are not yet included in standard catalogs due to a lack of techniques for estimating the second seismic moments with little user involvement.

Observed seismograms are generated by convolution of instrument response, seismic wave propagation effects, and earthquake source terms. To estimate source properties such as directivity and rupture size, the path and instrument effects should be removed from the data. This is often done by deconvolving seismograms of the analyzed (target) earthquake with an empirical Green's function (eGf) given by seismograms of suitable small collocated events (e.g. Hartzell, 1978; Hough & Dreger, 1995; Hutchings & Wu, 1990; Mueller, 1985; Ross & Ben-Zion, 2016). Although eGfs can effectively account for the path and site effects, it is difficult to find a good eGf with collocated hypocenters and almost identical focal mechanisms (FMs) as the target earthquakes. The differences in the FMs between the target event and eGf can corrupt the ASTFs for stations in various directions, producing poor station coverage and biased estimation of source properties. In addition, Calderoni et al. (2012), Calderoni et al. (2015) showed that if the eGf events have directivity effects in the frequency band of interest, this can result in apparent directivity of the target event. Ross and Ben-Zion (2013) demonstrated with synthetic calculations that small isotropic source terms can

produce errors in derivations of FMs constrained to be pure double-couples. Therefore, using a single eGf may bias the results if the eGf has nongeneric source effects such as directivity or a tensile component. In this paper, we develop a semiautomated technique for estimating second-degree seismic moments using a weighted stack of eGfs to improve the FM and suppress nongeneric source effects. The method is applied to derive source properties of small to moderate earthquakes in southern California.

Theoretical and numerical simulation results indicate that ruptures on a bimaterial fault may have a statistically preferred propagation direction related to the velocity contrast across the fault (e.g., Andrews & Ben-Zion, 1997; Ben-Zion & Huang, 2002; Di Bartolomeo et al., 2010; Ranjith & Rice, 2001; Weertman, 1980). Simulations of bimaterial ruptures on an interface governed by slip-weakening friction produced bilateral ruptures for various cases (e.g., Andrews & Harris, 2005; Harris & Day, 1997). However, large parameter-space studies with slip-weakening friction (e.g., Brietzke et al., 2009; Shi & Ben-Zion, 2006), slip- and velocity-dependent friction (Ampuero & Ben-Zion, 2008) and rate-state friction (Erickson & Day, 2016) showed that bimaterial ruptures tend to have preferred directivity for wide ranges of conditions. Recent high-resolution laboratory experiments of bimaterial ruptures have led to the same conclusion (Shlomai & Fineberg, 2016).

Since directivity in large earthquakes can significantly amplify the ground motion and cause more damage at sites in the forward direction, it is important to test the proposed connection between velocity contrast across faults and rupture directivity with *in situ* data. Several observational analyses of earthquakes directivities using source spectra and amplitudes of seismograms in different directions provided evidence for preferred rupture directions that are consistent with expectations associated with the local velocity contrasts (e.g., Calderoni et al., 2015; Kane et al., 2013; Kurzon et al., 2014; Lengliné & Got, 2011; Ross & Ben-Zion, 2016; Wang et al., 2014; Wang & Rubin, 2011). Similar inferences were made based on less direct observations associated with along-strike asymmetry of aftershocks (e.g., Lengliné & Ampuero, 2015; Rubin & Gillard, 2000; Zaliapin & Ben-Zion, 2011) and across-fault damage asymmetry (e.g., Dor et al., 2006, 2008; Lewis et al., 2005; Mitchell et al., 2011; Share, Allam, et al., 2019). Opposite propagation directions of eight earthquakes along the Parkfield section of the San Andreas fault, with events around Middle Mountain including the 1934 and 1966  $M$  6 earthquakes propagating to the southeast and events around Gold Hill including the 2004  $M$  6 earthquake propagating to the northwest, led Harris and Day (2005) to argue that bimaterial faults do not affect rupture directions. However, detailed tomographic imaging indicate a clear reversal of the velocity contrast between these different fault sections (Eberhart-Phillips & Michael, 1993; Thurber et al., 2006). This and additional studies at Parkfield with larger data sets (e.g., Kane et al., 2013; Lengliné & Got, 2011) imply consistency between the observed opposite rupture directions and expectations for bimaterial ruptures.

It is important to continue to test with improved methods and data whether earthquakes have directivities that correlate with velocity contrasts across faults. In the present paper we develop a semiautomated analysis procedure to estimate rupture directivities and related finite fault attributes based on second seismic moments of small to moderate earthquakes. Compared with conventional methods that measure source spectra and corner frequencies (e.g., Abercrombie, 2015; Baltay et al., 2010; Goebel et al., 2015; Houston & Kanamori, 1986; Prieto et al., 2004; Shearer et al., 2006; Uchide et al., 2014), the second seismic moments method directly resolves simple finite source properties, including rupture length, width, source duration, centroid rupture velocity, and directivity, without assuming a rupture model. The semiautomated method is applied to data recorded by stations of Southern California Seismic Network (SCSN) for 41 earthquakes in the magnitude range 3.5–5.2 and provides stable results on estimate rupture velocities and directivities for 28 events. The remaining 13 target earthquakes are not resolvable due to insufficient station coverage. Corresponding stress drop estimates for the 28 events (including upper and lower bounds) are determined using various constraints on the rupture dimensions obtained by the second moment inversions.

## 2. Data

The employed data are associated with a set of 41 well-recorded target earthquakes observed by seismic stations from several networks, including the Anza network (AZ) (Vernon, 1982), the Plate Boundary Observatory Borehole network (PB), the Southern California Seismic network (CI) (Southern California Earthquake Data Center (SCEDC), 2013), and the University of California, Santa Barbara Engineering

**Table 1**  
*Target Events Analyzed in This Study*

No.	Date	Event ID	Latitude	Longitude	Depth (km)	M	Strike	Dip	Rake
1	2016-06-10	37374687	33.44031	-116.43520	12.433	5.19	303	66	179
2	2014-03-29	15481673	33.90461	-117.95333	6.005	5.10	130	55	165
3	2010-06-13	10701405	33.39017	-116.39906	7.856	4.90	331	83	-178
4	2013-01-11	15296281	33.50576	-116.45860	9.954	4.70	315	76	-167
5	2014-07-05	15520985	34.27669	-117.02524	7.972	4.58	306	72	-179
6	2018-05-08	38167848	34.02100	-116.78521	13.535	4.49	277	58	132
7	2012-08-08	15189073	33.91105	-117.78970	9.532	4.46	130	86	-174
8	2012-08-08	15189281	33.91018	-117.78671	9.318	4.45	121	71	180
9	2018-08-15	38245496	33.49083	-116.78945	4.114	4.43	344	90	171
10	2014-01-15	11413954	34.14743	-117.44549	3.864	4.43	303	63	178
11	2018-08-29	38038071	34.12779	-117.78223	4.717	4.41	315	74	-162
12	2015-12-30	37507576	34.19584	-117.41829	8.490	4.40	308	81	178
13	2016-01-06	37510616	33.97150	-116.88264	15.995	4.39	307	54	140
14	2010-01-16	10530013	33.94010	-117.01966	15.099	4.28	327	84	178
15	2010-01-12	14571828	33.97229	-116.87233	9.069	4.27	345	66	171
16	2008-05-01	10321561	33.44600	-116.43665	8.615	4.19	316	65	168
17	2014-03-29	15483001	33.95630	-117.89722	6.615	4.14	114	63	-168
18	2011-09-14	11006189	33.96212	-117.06751	16.492	4.14	333	57	-172
19	2008-10-02	14396336	34.09154	-116.97180	14.984	4.14	98	44	96
20	2012-08-29	15207433	33.90630	-117.79178	9.016	4.13	128	71	-178
21	2008-11-17	14403732	33.50959	-116.84798	11.557	4.11	314	87	-164
22	2010-02-13	10541957	34.01192	-117.18447	8.832	4.10	174	59	-143
23	2008-05-09	14367532	33.44844	-116.44030	7.848	4.06	314	78	175
24	2015-09-16	37243591	34.13885	-116.85416	11.858	4.00	304	57	-157
25	2012-06-14	15164105	33.91156	-117.78737	9.694	3.99	130	72	179
26	2008-06-23	14376612	34.05278	-117.24309	15.231	3.99	339	63	-177
27	2009-04-24	10399889	33.90450	-117.79791	0.004	3.98	114	76	172
28	2018-01-25	38092312	33.74950	-117.50117	10.711	3.97	273	43	106
29	2018-04-26	37924223	33.38645	-116.29694	11.293	3.94	288	80	169
30	2016-12-28	37772688	34.15459	-116.70373	12.700	3.92	137	89	-175
31	2012-10-28	15237073	33.70513	-116.80654	16.852	3.87	297	38	138
32	2018-04-23	37920791	33.92635	-116.31881	9.570	3.87	333	75	176
33	2016-02-16	37524376	34.29963	-116.86221	5.522	3.87	303	75	-178
34	2009-04-16	14444832	33.25538	-116.41990	3.221	3.86	318	72	171
35	2014-05-19	15503377	34.25475	-116.82586	8.448	3.84	317	84	179
36	2012-04-28	15141521	34.24089	-117.43179	12.971	3.82	283	43	102
37	2015-07-25	37213455	34.09732	-117.44811	4.849	3.81	308	77	175
38	2013-09-20	11366994	33.35229	-116.39017	12.175	3.80	334	76	179
39	2008-07-29	14384052	33.94852	-117.81039	13.900	3.80	125	56	163
40	2011-05-27	14992276	34.22025	-117.05263	0.728	3.80	286	81	-166
41	2014-08-15	15538561	34.29708	-116.44877	10.351	3.80	345	83	-177
42	2016-06-10	37377079	33.46393	-116.41829	10.404	3.46	172	68	-154

Note. Dates are formatted as year-month-day.

Seismology Network (SB) (Table 1; Figure 1). Most of these events occurred near the San Jacinto Fault Zone (SJFZ), the Elsinore Fault Zone (EFZ) or the Eastern California Shear Zone (ECSZ) (Hart et al., 1989), and they have predominantly right lateral strike-slip FMs. For each target earthquake, tentative eGf candidates are selected from the relocated catalog of Hauksson et al. (2012; extended to later years) with magnitudes 1.5 to 2.5 units smaller than the target event and hypocentral separation of no more than 5 km from the target event. The details of how the eGf candidates are qualified and processed are documented in the next section.

For the analyzed target and eGf events, we only use broadband and strong motion records (HH and HN channels) with sampling rates of 100 Hz and higher. HN channels are integrated in the frequency domain from accelerations to velocities. A bandpass filtering with corner frequencies at 0.5 and 20 Hz is then performed on the waveforms to suppress the noise associated with ocean tides, wind, and various other natural and anthropogenic noise sources (e.g. Hillers et al., 2013; Inbal et al., 2018; Johnson et al., 2019; Meng & Ben-

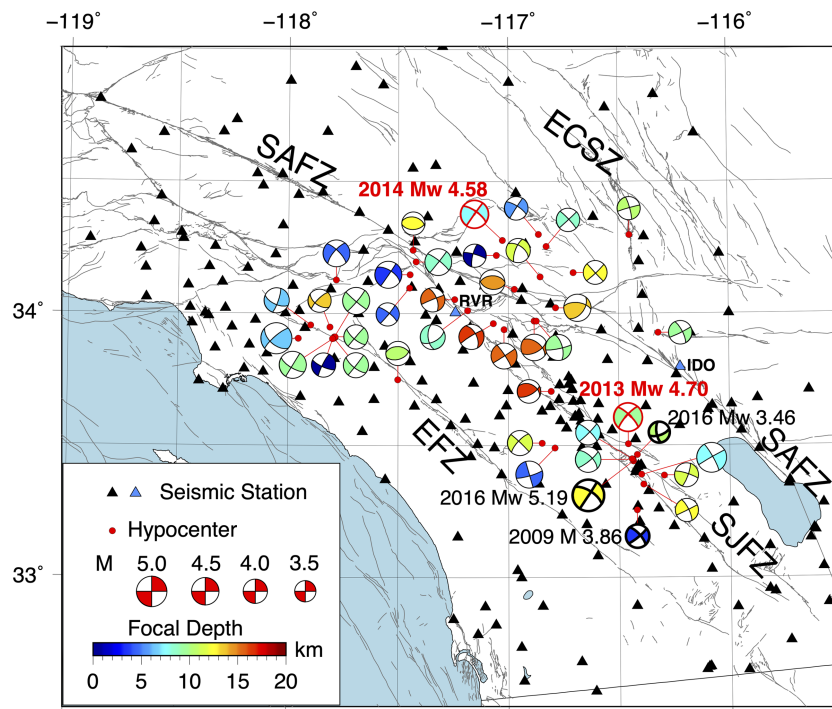


**Figure 1.** A map of the Southern California plate boundary region. SCSN and ANZA seismic stations used in this study are denoted by black triangles. The analyzed events are indicated by red circles with associated beach balls showing focal mechanisms, magnitudes (size), and focal depth (colors). Example stations IDO and RVR are denoted by blue triangles. Example events used to illustrate results are highlighted by bold beach balls and texts.

Zion, 2018). We primarily use the transverse component to get relatively clean  $SH$  wave data and the vertical component to get  $P$  wave data. The deconvolution results of  $SH$  wave data in general have significantly better performance in waveform fitting than either the  $P$  or  $SV$  waves. To improve the computational efficiency, we exclude records with low signal-to-noise ratio (SNR) and clipped waveforms detected by the technique of Yang and Ben-Zion (2010). Broadband records are preferred when both HH and HN channels are available and not clipped.

### 3. Methods

#### 3.1. Mathematical Representation of the Second Seismic Moments

Following McGuire (2004, 2017), we make the simplifying assumption that the spatial variations in moment rate of an earthquake can be described as:

$$\begin{aligned}\underline{\underline{M}}(\underline{r}, t) &= \underline{\underline{M}}\dot{f}(\underline{r}, t), \\ \int \dot{f}(\underline{r}, t) dV dt &= 1,\end{aligned}\quad (1)$$

where  $\underline{\underline{M}}$  is the seismic moment tensor,  $\underline{\underline{M}}\dot{f}(\underline{r}, t)$  is the moment rate function, and  $\dot{f}(\underline{r}, t)$  is a normalized scalar function (integrated to unity) that describes the spatial and temporal distribution of moment release along the fault. Integrating  $\dot{f}(\underline{r}, t)$  over the entire source volume gives the normalized source time function (STF).

The first seismic moments of an earthquake are the centroid location  $\underline{r}_0$  and time  $t_0$  representing the spatio-temporal means of its moment release

$$\begin{aligned}\underline{r}_0 &= \iiint \dot{f}(\underline{r}, t) \underline{r} dV dt, \\ t_0 &= \iiint \dot{f}(\underline{r}, t) t dV dt.\end{aligned}\quad (2)$$

The second seismic moments are mathematical representations to capture the overall kinematic properties of a rupture that are well constrained by the far-field seismic waveforms. The second moments are defined as

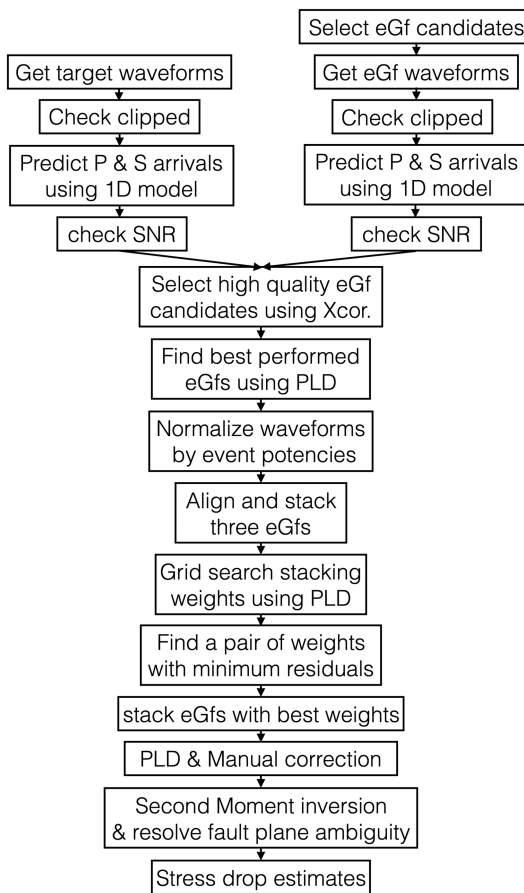


**Figure 2.** A flow diagram summarizing the main steps of the semiautomated method.

where  $x_c(\hat{n})$  is the spatial extent of the rupture in the direction  $\hat{n}$ . The characteristic rupture length  $L_c = \max(x_c(\hat{n}))$  is the largest eigenvalue of the special moment and the characteristic rupture width  $W_c$  is the second largest eigenvalue. The directivity ratio ( $0 \leq \text{dir} \leq 1$ ) is defined as

$$\begin{aligned} x_c(\hat{n}) &= 2\sqrt{\hat{n}^T \underline{\hat{\mu}}^{(2,0)} \hat{n}}, \\ \tau_c &= 2\sqrt{\underline{\hat{\mu}}^{(0,2)}}, \\ \underline{v}_0 &= \frac{\underline{\hat{\mu}}^{(1,1)}}{\underline{\hat{\mu}}^{(0,2)}}, \end{aligned} \quad (4)$$

where  $V_c$  is the characteristic velocity. For a perfect symmetric bilateral rupture  $\text{dir} = 0$ , while for a uniform unilateral rupture  $\text{dir} = 1$ .

### 3.2. Qualifying eGf Candidates

The approach of McGuire (2004, 2017) requires heavy user involvement. Here we develop a semiautomated technique which automates most of the steps. The methodology is summarized in a flowchart diagram (Figure 2) and illustrated using seismic data from a 2014  $M_w$  4.58 target event (earthquake No. 5 in Table 1 and shown in Figure 1).

As mentioned, for each target event we select eGf candidates with magnitudes 1.5 to 2.5 smaller than that of the target and hypocentral separations of no more than 5 km. The selection of eGf candidates is usually limited to foreshocks and aftershocks occurring 1 month before and after the target earthquake (McGuire, 2004). However, here this is done using the relocated catalog of Hauksson et al. (2012, extended to later years) for the period 2009 to 2018 to maximize the number of eGf candidates. We use data recorded by seismic stations at hypocentral distances less than 120 km to avoid the noisier records from stations at larger distances. We average the community velocity model for Southern California (CVM-S4.26; Lee et al., 2014) to a 1-D velocity model and use this to estimate the  $P$  and  $S$  arrivals. These estimates are improved by maximizing

the second-order space and time moments of the normalized moment-rate distribution function (Backus, 1977a, 1977b):

$$\begin{aligned} \underline{\hat{\mu}}^{(2,0)} &= \iiint \hat{f}(\underline{r}, t)(\underline{r}-\underline{r}_0)^T(\underline{r}-\underline{r}_0)dVdt, \\ \underline{\hat{\mu}}^{(0,2)} &= \iint \hat{f}(\underline{r}, t)(t-t_0)(t-t_0)dVdt, \\ \underline{\hat{\mu}}^{(1,1)} &= \iint \hat{f}(\underline{r}, t)(\underline{r}-\underline{r}_0)(t-t_0)dVdt, \end{aligned} \quad (3)$$

where  $\underline{r}_0$  and  $t_0$  are column vectors representing the centroid location and time defined in equation (2). The hat signs in equation (3) indicate that these second moments are central moments taken about the centroid. The integrals are taken over the entire source volume and earthquake duration (McGuire et al., 2001; Backus, 1977a, 1977b). The second spatial moment  $\underline{\hat{\mu}}^{(2,0)}$  is a 3 by 3 symmetric tensor (six unique elements) associated with the rupture extent; the temporal moment  $\underline{\hat{\mu}}^{(0,2)}$  is a scalar (one unique element) associated with rupture duration; and the mixed moment  $\underline{\hat{\mu}}^{(1,1)}$  is a column vector (three unique elements) associated with rupture propagation (McGuire, 2004, 2017).

The characteristic rupture dimension  $x_c(\hat{n})$ , characteristic rupture duration  $\tau_c$ , and centroid rupture velocity  $\underline{v}_0$  are defined as

$$\begin{aligned} x_c(\hat{n}) &= 2\sqrt{\hat{n}^T \underline{\hat{\mu}}^{(2,0)} \hat{n}}, \\ \tau_c &= 2\sqrt{\underline{\hat{\mu}}^{(0,2)}}, \\ \underline{v}_0 &= \frac{\underline{\hat{\mu}}^{(1,1)}}{\underline{\hat{\mu}}^{(0,2)}}, \end{aligned} \quad (4)$$

where  $x_c(\hat{n})$  is the spatial extent of the rupture in the direction  $\hat{n}$ . The characteristic rupture length  $L_c = \max(x_c(\hat{n}))$  is the largest eigenvalue of the special moment and the characteristic rupture width  $W_c$  is the second largest eigenvalue. The directivity ratio ( $0 \leq \text{dir} \leq 1$ ) is defined as

$$\begin{aligned} v_c &= \frac{L_c}{\tau_c}, \\ \text{dir} &= \frac{|\underline{v}_0|}{v_c}, \end{aligned} \quad (5)$$

the SNR on each zero crossing of waveforms within the  $\pm 1$  s window around the theoretical arrival (Li & Peng, 2016). The SNR is estimated using a ratio of two 1 s moving averages after and before the improved *P/S* arrival estimate, and eGf waveforms with  $\text{SNR} \leq 5$  are discarded.

In the next step, we evaluate the quality of eGf candidates using cross-correlation and deconvolution. We first band-pass filter the *T* component raw waveforms from 0.5 to 2 Hz and cut 10 s long *S* phases (2 s before and 8 s after the improved arrival estimate) to compute the maximal cross-correlation coefficients (CCs) of the target earthquake and its eGf candidates (Figure S1a in the supporting information). These waveforms are only employed for computing CCs, not for deconvolution. We then estimate the quality of the eGf candidates by their average CCs and the numbers of available records (Figure S1b). To promote computing efficiency, we only perform the time-consuming deconvolution analysis for no more than 10 eGf candidates with the highest average CC's. Figure S1c shows the cross-correlation coefficient functions of the *S* phases of the target and one eGf (SCSN event ID: 15521073) at stations IDO and RVR. The pulses around the maximum CCs are similar to the ASTFs computed from the waveform deconvolution of the target earthquake by its eGf, since the phase terms of the deconvolution and cross correlation are identical. Therefore, the CCs are higher at stations with ASTFs of a single pulse, which are more likely to be in the rupture propagation direction. For the 2014  $M_w$  4.58 target event, the CCs are generally higher at stations in the azimuth range 16–145°, indicating a possible directivity toward the southeast. This is substantiated by further analyses in section 3.3.

In the calculation of the deconvolution, the window lengths for the *P* and *S* phases are 256 and 512 samples with a sampling rate of 100 Hz. The qualities of the eGf candidates are finalized using the projected Landweber deconvolution (PLD) algorithm (Bertero et al., 1997; Lanza et al., 1999), which performs the deconvolution with moment release restricted to a series of increasing-length time intervals and analyzes the misfit as a function of the interval length. Example of the PLD processing step is shown by Figure 3 with the SH phase of the 2014  $M_w$  4.58 event and its best performing single eGf at station RVR (Figure 1). The deconvolved ASTF is estimated using PLD with nonnegative and limited duration constraints. The normalized misfit (Figure 3c), calculated as the L2 norm of the difference of the observed and fitted SH waves normalized by the L2 norm of the observed SH, decreases monotonically as longer permissible time intervals allow moment release to occur. The optimized duration of the ASTF is picked at the interval where the misfit is small enough and the tradeoff curve is relatively flat. The flat stage indicates a relative stable ASTF estimate that is not significantly affected by a small perturbation in the permitted duration. The selection of duration is automated by selecting the smallest duration with normalized misfit  $\leq 0.3$  and its time derivative at local maxima (close to zero). The optimized ASTF with respect to the duration picked in Figure 3c is shown in Figure 3d.

The deconvolution is sensitive to the accuracy of the onsets of phases especially for eGfs. We therefore perform a grid search on the zero-crossings of the target and eGf waveforms within a short time window (i.e.,  $\pm 0.5$  s) around the improved *P/S* picks and run PLD for each pair of zero crossings. The *P/S* picks are then further refined to the zero crossings with the best fit of the target waveform. The performances of eGf candidates are determined from high to low by the total number of stations with acceptable waveform fits in the deconvolution. This step of evaluating each eGf is relatively time-consuming and takes most of the computing time, because of the grid search and the time domain deconvolution, but it is automated in our analysis procedure.

### 3.3. Weighted Stack of eGfs

To ensure good station coverage, and to stabilize the second seismic moment inversion for target earthquakes, the measurements of apparent durations are needed at as many stations as possible. A better represented eGf is therefore required and obtained in this study by stacking several eGf candidates with the best-performing eGf. Recent observational studies demonstrated that directivity and tensile components of faulting may be common features of small events (e.g., Calderoni et al., 2015; Kane et al., 2013; Kurzon et al., 2014; Ross & Ben-Zion, 2013). If such features are present in the eGf, this would bias the results derived for the target events. Stacking several eGfs can suppress such effects, reduce the background noise, and produce a more generic average eGf if there are variations. A noise-free eGf with a double couple source mechanism is a linear combination of five independent Green's function components. The combination coefficients depend on the strike, dip and rake of the rupture. Therefore, a linear combination of five

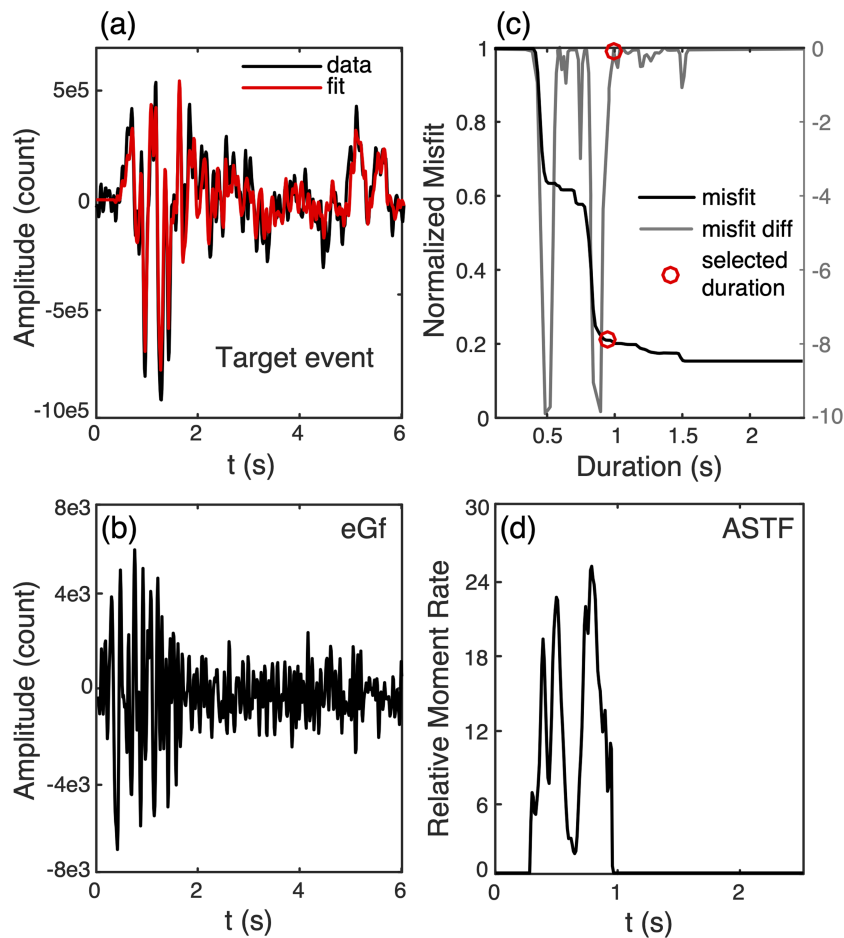


**Figure 3.** An example of PLD for the  $M_w$  4.58, 2014 at station RVR. (a) The  $S$  phase and its fit in the transverse component. (b) The  $S$  phase of the eGf in the transverse component. (c) The black curve shows the normalized misfit and the gray curve shows its time derivative with different durations of the ASTF. The red circles denote the selected duration for the deconvolution. (d) The deconvolved ASTF.

collocated and well-aligned eGfs with independent FMs of similar sizes can recover an eGf with any FM. To reduce the computational complexity, we stack the best performing eGfs with only two additional eGfs with good performance in the deconvolution.

After we find three best qualified eGfs for the target event, that is, 2014  $M_w$  4.58 earthquake, we normalize the eGfs individually by the seismic potency calculated from the quadratic potency-magnitude scaling relation of Ben-Zion and Zhu (2002). The waveforms of these eGfs are sufficiently similar to be aligned using cross-correlation at most stations. Figure 4 shows the  $SH$  phases of the target, three aligned and normalized eGfs, associated grid search of the stacking weights and corresponding deconvolution results (Figures 4c and 4f) of the 2014  $M_w$  4.58 target event at station RVR and IDO. The eGfs are aligned by cross-correlations and the refined arrivals of  $S$  waves are denoted by blue circles. The amplitude differences at various wiggles are likely primarily because of FM differences. We perform a grid-search to determine the weights of eGfs 2 and 3 with a 0.1 spacing in the range from -3 to 3. The weight of the best performing eGf 1 is fixed as 1 without losing generality. The duration of ASTF is fixed as the duration picked in the PLD for the grid search for the best-performing eGf 1, and that value is used in the PLD to calculate the misfit to the observed waveforms for each pair of weights. The white cross at the local minimum of Figure 4b denotes the best pair of weights for the stacking coefficients. Figure 4c shows the weighted stacked eGfs with the selected pair of weights, the resulting ASTFs, and waveform fits. We limit the stack to three eGfs to achieve improved performance but retain computation efficiency. Stacking more than three eGfs will dramatically increase the search

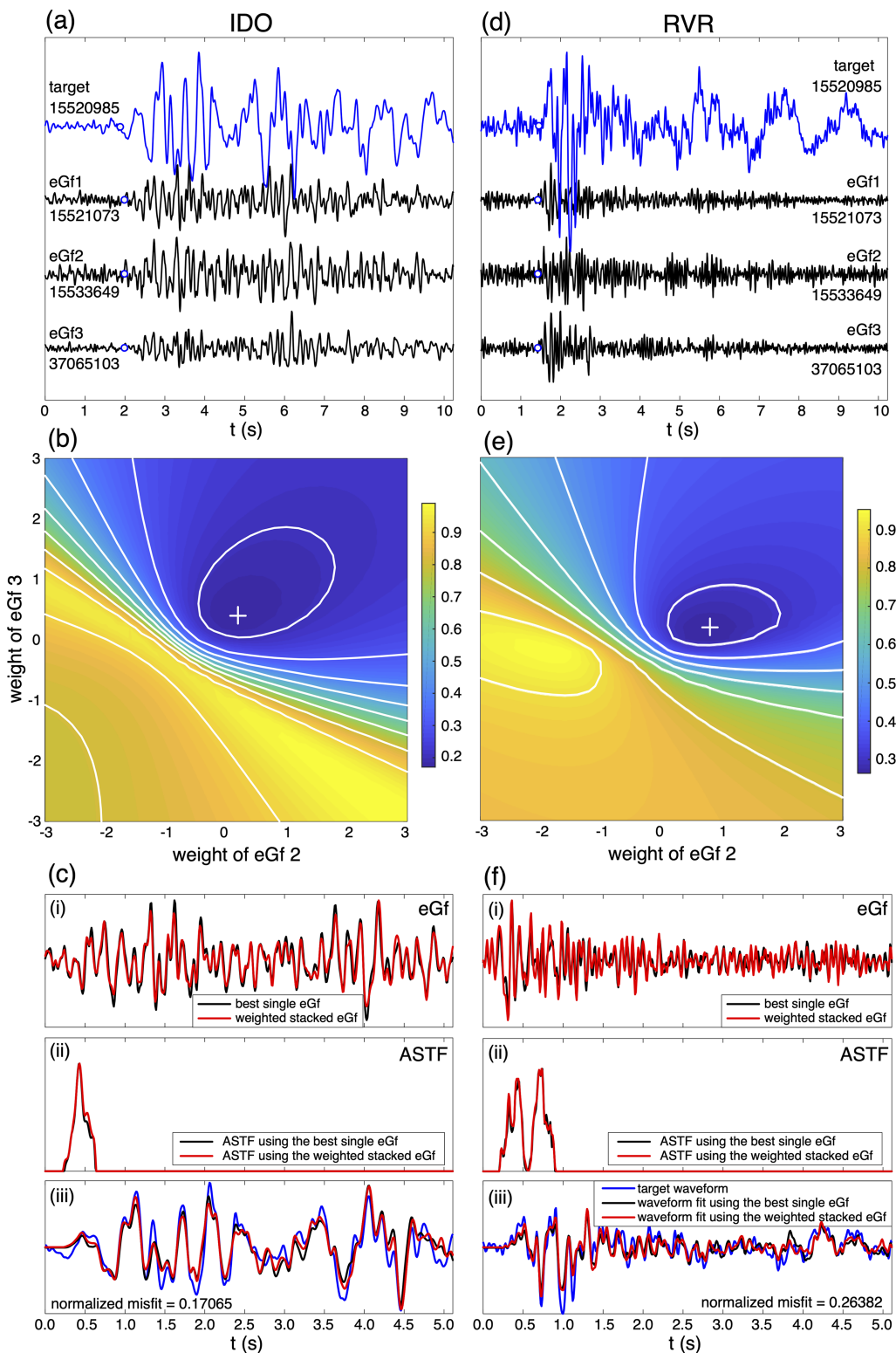


**Figure 4.** Weighted stack of eGfs at example stations IDO and RVR in Figure 1 for the  $M_w$  4.58, 2014 target earthquake. All waveforms are  $S$  phases in the transverse component. (a) Waveforms of the target events and three best performing eGfs recorded by station IDO. The eGf 1 is the best performing eGf and its weight is fixed as 1. (b) Grid search for stacking weights for eGfs 2 and 3. The white crosses denote the best pair of weight for station IDO. The color displays the normalized misfit in the PLD with the waveforms of the target event and stacked eGf. (c) (i) Waveforms of best performing eGf and weighted stacked eGf, (ii) ASTFs, (iii) waveform of the target event and its fit using the weighted stacked eGf and best single eGf at station IDO. (d)–(f) Similar to (a)–(c) but for station RVR. The blue circles in (a) and (c) indicate the refined arrivals of  $S$  phases.

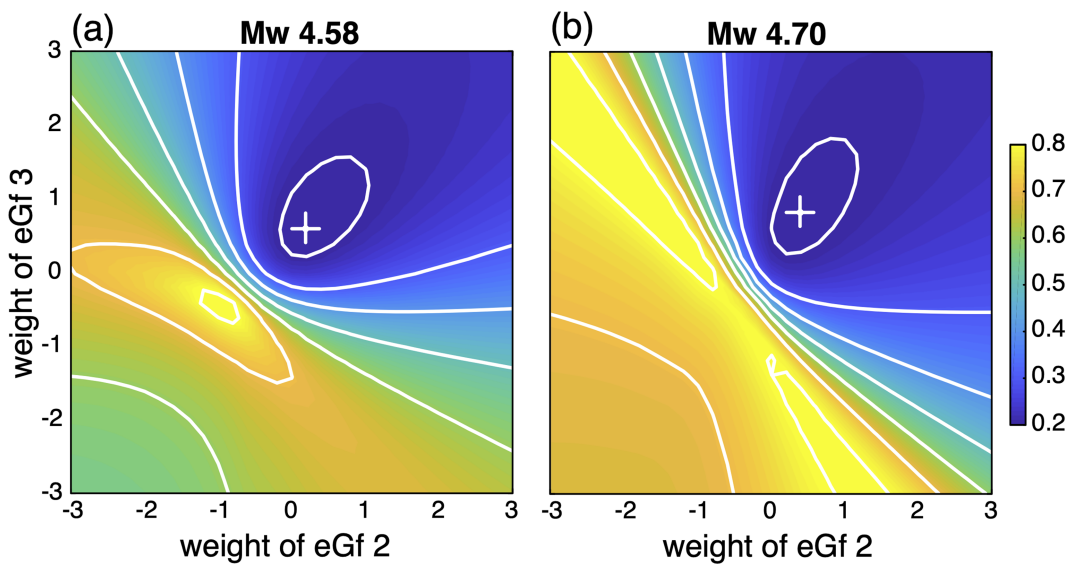


**Figure 5.** Averaged misfit distribution for different pairs of weights for all used stations in analyses of (a) the 2014  $M_w$  4.58 and (b) the 2013  $M_w$  4.70 target events. The bold white crosses denote the pair of weights with the best waveform fit.

complexity but could be implemented with longer computing time. Corresponding results at another example station IDO are shown in Figures 4d–4f. The best pairs of weights are different at various stations indicating the aleatory variability of the measurements. The ASTFs in Figures 4c and 4f are significantly different because station RVR and IDO are at different directions to the rupture propagation direction and have different directivity effects.

The misfits as functions of weights of eGf 2 and 3 (Figures 4b and 4e) are stacked and averaged iteratively to find the best pair of weights for all stations. In the first iteration, we stack and average the misfits for all stations to obtain a pair of weights with least misfit. Stations with misfit  $>0.3$  for the selected weights are discarded. In the following iterations, we stack and average the misfits for the remaining stations and find a new pair of weights with least misfit. We repeat this process until no more stations are excluded. The iterative process is stable and usually converges in three iterations. Figure 5 presents the final averaged misfit patterns for the 2014  $M_w$  4.58 and the 2013  $M_w$  4.70 events with the selected weights denoted by the white crosses. The average misfit is significantly smaller using the weighted stacked eGf compared with a single eGf.

The characteristic durations, ASTFs, and normalized misfits for the 2014  $M_w$  4.58 event at different stations are presented in Figures 6a–6c. The ASTFs (Figure 6b) show systematic variations with the back azimuth that indicate a significant directivity to the SE. We also note that there are two clear pulses in the ASTFs for the approximate azimuth range 225–320°, suggesting the existence of two major subevents. Figure 6c shows the normalized misfit before and after using the weighted stack. The stacked eGf results in 36 accepted measurements for this target event and gives strong azimuthal and take-off angle coverage for the second moment inversion. The employed weighted stack technique results in a larger number of accepted measurements compared with using a single eGf (26 measurements in this case), which improves the stability of the results. Figures 7a–7c show corresponding results for a 2013  $M_w$  4.70 earthquake on the San Jacinto fault zone. The ASTFs for this event indicate moderate directivity to the NW and again suggest (ASTFs in the approximate azimuth range 69–225°) the existence of two main subevents. These inferences for the 2013  $M_w$  4.70 are consistent with earlier results of Ross and Ben-Zion (2016) and McGuire (2017). Figure S2 presents the waveforms and data fit of these two example target events. The good waveform fits indicate the high quality of weighted stacked eGfs and good ASTF estimates. Figure S3 illustrates the characteristic durations, ASTFs, and normalized misfits of the 2016  $M_w$  5.19 earthquake in the Trifurcation area, which shows a strong directivity toward the northwest. This is consistent with previous results of Ross and Ben-Zion (2016) and Ross et al. (2017). Figures S4 and S5 present additional results for the 2009,  $M$  3.86 and 2016,  $M$  3.46 earthquakes.

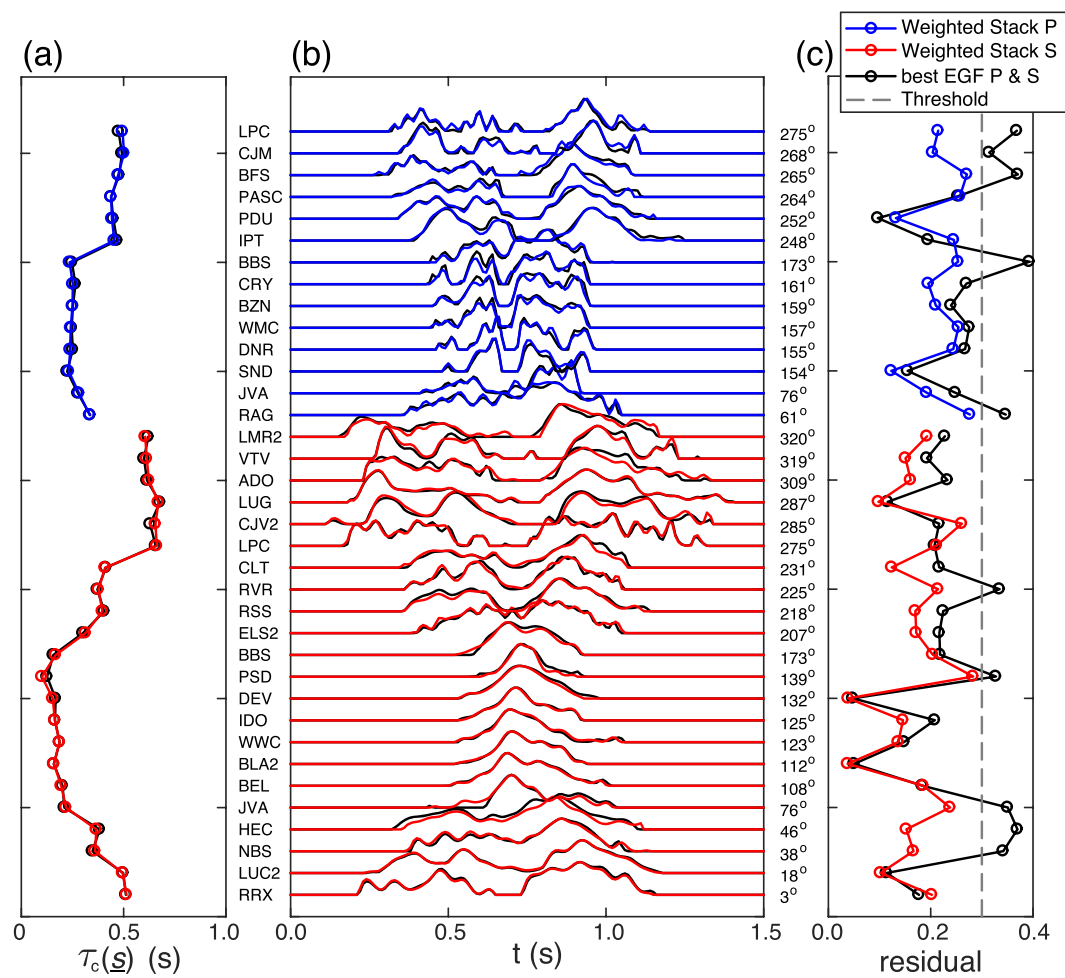


**Figure 6.** (a) Characteristic durations, (b) ASTFs, and (c) normalized misfits for best performing and weighted stacked eGFs for the 2014  $M_w$  4.6 event.  $P$  and  $S$  phases are in the vertical and transverse directions, respectively. Texts give station names and corresponding back azimuths for all stations.

### 3.4. Inversion Scheme for Second Moments

The second moments are related to the azimuthal variations in the duration of ASTFs at a given station as

$$\begin{aligned}\hat{\mu}^{(0,2)}(\underline{s}) &= \hat{\mu}^{(0,2)} - 2\underline{s} \cdot \hat{\mu}^{(1,1)} + \underline{s} \cdot \hat{\mu}^{(2,0)} \underline{s}, \\ \tau_c(\underline{s}) &= 2\sqrt{\hat{\mu}^{(0,2)}(\underline{s})},\end{aligned}\quad (6)$$

where  $\hat{\mu}^{(0,2)}(\underline{s})$  is the apparent temporal moment measured at each station,  $\underline{s}$  is the slowness of  $P$  or  $S$  phase in the source region, and  $\tau_c(\underline{s})$  is the apparent characteristic duration (McGuire, 2004, 2017). The slowness vectors can be easily obtained with the 1-D ray tracing technique. Employing the FM of the target earthquake,  $\hat{\mu}^{(2,0)}$  becomes a 2 by 2 symmetric tensor (three unique elements);  $\hat{\mu}^{(0,2)}$  is a scalar (one unique element); and  $\hat{\mu}^{(1,1)}$  becomes a column vector (two unique elements) by projecting equation (6) onto the 2-D fault plane. The number of unknown parameters can therefore be reduced from 10 to 6. Ignoring the fault perpendicular direction, equation (6) can be rewritten as

$$\begin{aligned}\hat{\mu}^{(0,2)}(\underline{s}) &= [s_1^2 \quad 2s_1s_2 \quad s_2^2 \quad -2s_1 \quad -2s_2 \quad 1] \cdot \underline{x} \\ \underline{x} &= \left[ \begin{array}{c} \hat{\mu}_{11}^{(2,0)} \quad \hat{\mu}_{12}^{(2,0)} \quad \hat{\mu}_{22}^{(2,0)} \\ \hat{\mu}_1^{(1,1)} \hat{\mu}_2^{(1,1)} \hat{\mu}^{(0,2)} \end{array} \right]^T\end{aligned}\quad (7)$$

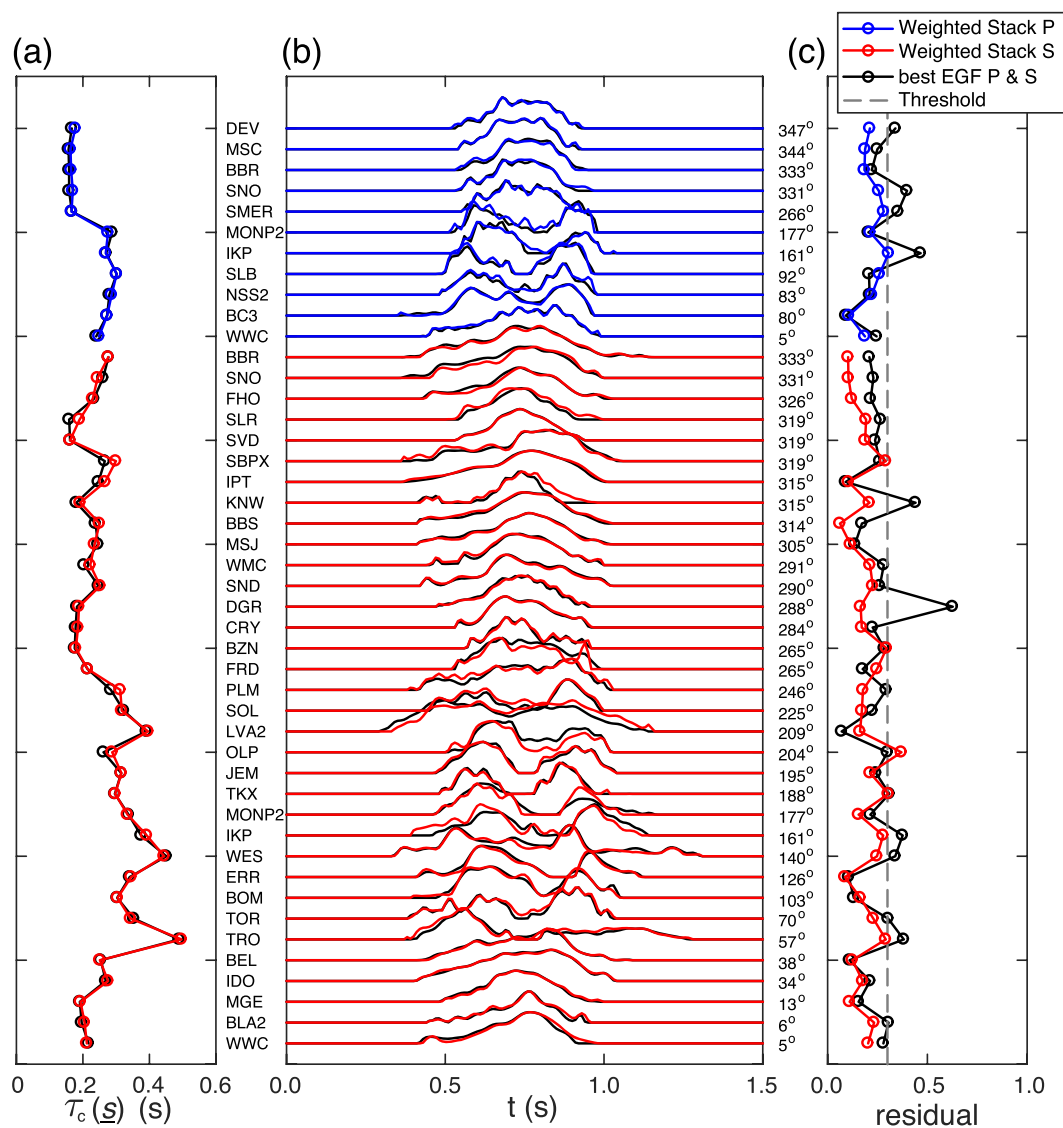


**Figure 7.** (a) Characteristic durations, (b) ASTFs, and (c) normalized misfits for best performing eGf and weighted stacked eGf for the 2013  $M_w$  4.70 event.  $P$  and  $S$  phases are in the vertical and transverse directions, respectively. Texts give station names and corresponding back azimuths for all stations.

where  $s_1$  (along strike) and  $s_2$  (along dip) are parallel to the fault plane. With observed durations of ASTFs at various stations, one can build a linear system for inversion

$$\underline{b} = \underline{\underline{A}}\underline{x}, \quad (8)$$

where  $\underline{b}$  is a column vector consisting of apparent durations  $\widehat{\mu}^{(0,2)}(s)$  and  $\underline{\underline{A}}$  is the matrix associated with the slowness components in equation (7). Equations (7) and (8) are subject to

$$\begin{bmatrix} \widehat{\mu}^{(0,2)} & \widehat{\mu}^{(1,1)T} \\ \widehat{\mu}^{(1,1)} & \widehat{\mu}^{(2,0)} \end{bmatrix} \geq 0, \quad (9)$$

which enforces the physical constraint of a nonnegative source volume. The problem is solved through convex optimization (Boyd & Vandenberghe, 2004; Grant & Boyd, 2008, 2014; Vandenberghe & Boyd, 1996) as

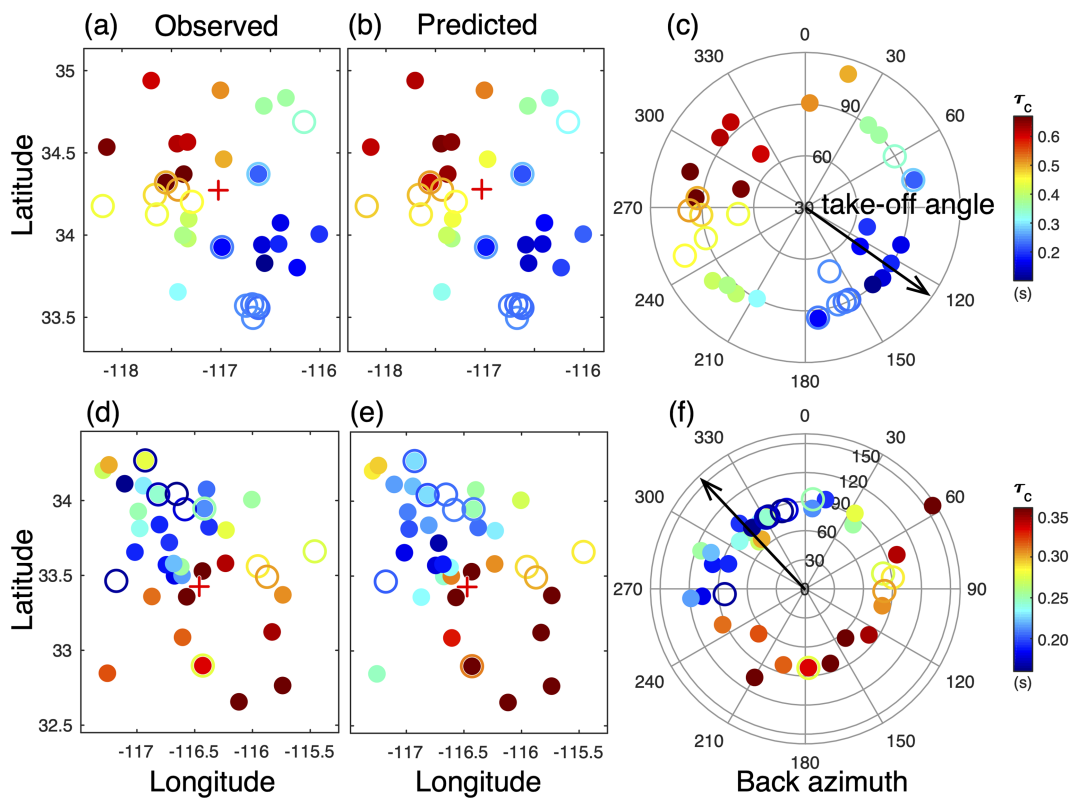


**Figure 8.** (a, b) Observed and predicted characteristic durations at receivers for the 2014  $M_w$  4.58 earthquake, respectively. The colored dots and circles denote the apparent durations  $\tau_c(\text{s})$  of  $S$  and  $P$  phases. (c) Azimuthal and take-off angle distribution of all accepted measurements. The black arrow denotes the horizontal component of the optimal rupture directivity. Panels (d)–(f) are similar to panels (a)–(c) but for the 2013  $M_w$  4.70 target event.

$$\begin{aligned} & \min \|b - \underline{\mathcal{A}} \cdot \underline{x}\|_2 \\ & \text{subject to } \begin{bmatrix} \widehat{\underline{\mu}}^{(0,2)} \widehat{\underline{\mu}}^{(1,1)T} \\ \widehat{\underline{\mu}}^{(1,1)} \widehat{\underline{\mu}}^{(2,0)} \end{bmatrix} \geq 0, \\ & \text{and } \widehat{\underline{\mu}}^{(0,2)} \leq 2 \max(b). \end{aligned} \quad (10)$$

In practice, the least squares objective function is implemented using Schur complements (McGuire, 2017). In addition to the physical constraint, we require the second temporal moment to be less than twice the largest measurement of  $\widehat{\underline{\mu}}^{(0,2)}(\text{s})$ , which should be satisfied with a good station coverage (without significant azimuthal gap and with both up-going and down-going rays) of a target earthquake (Fan & McGuire, 2018).

Figure 8 shows the observed and predicted apparent  $\tau_c(\text{s})$  at all stations and the azimuthal and take-off angle distributions of the accepted stations using the weighted stacked eGf method for the target events 2014  $M_w$  4.58 and the 2013  $M_w$  4.70. The apparent  $\tau_c(\text{s})$  shows strong directivity for both of these target events. To resolve the fault plane ambiguity, we perform the second moment inversion using both possible rupture planes. The plane with smaller misfit to the observed apparent  $\tau_c(\text{s})$  values is determined as the actual rupture plane. In Figure 8c, there are no significant azimuthal gaps ( $>45^\circ$ ) and there are both up-going (take-off angle  $>90^\circ$ ) and down-going (take-off angle  $<90^\circ$ ) rays. The accepted fault plane for this event is parallel to both the SJFZ and SAFZ. The arrow toward the southeast (Figure 8c) indicates the rupture propagation

**Table 2**

Second Moment Inversion Results of the 2014  $M_w$  4.58 Event (ID: 15520985)

eGf type	$L_c$ (km)	$W_c$ (km)	$\tau_c$ (s)	$v_0$ (km/s)	Directivity ratio	Residual per degree of freedom (s)	Number of measurements
Single eGf	1.12	0.48	0.37	2.70	0.87	0.0278	26
Stacked eGf	1.12	0.50	0.37	2.73	0.89	0.0223	36

**Table 3**

Results for the Analyzed Event Using Weighted Stacked eGf.

Event ID	M	$L_c$ (km)	$W_c$ (km/s)	$\tau_c$ (s)	Directivity ratio	Stress drop (MPa)	Min stress drop (MPa)	Max stress drop (MPa)
37374687	5.19	1.77	0.82	0.294	0.846	20.90	3.14	177.87
10701405	4.90	1.16	0.36	0.108	0.504	58.82	10.14	1811.32
15296281	4.70	1.64	0.58	0.244	0.316	8.12	4.00	11.11
15520985	4.58	1.12	0.52	0.366	0.889	9.98	1.21	69.99
38038071	4.41	0.65	0.49	0.171	0.585	4.54	1.46	1362.45
37507576	4.40	0.73	0.32	0.172	0.632	21.75	2.46	82.01
10530013	4.28	0.29	0.19	0.074	0.551	44.83	10.59	-
14571828	4.27	0.48	0.13	0.094	0.432	57.02	2.42	870.14
10321561	4.19	0.56	0.14	0.067	0.247	74.84	22.97	235.98
15483001	4.14	0.54	0.17	0.058	0.543	42.66	3.73	572.82
15207433	4.13	0.55	0.17	0.066	0.358	38.73	2.48	276.84
14403732	4.11	0.44	0.18	0.042	0.044	41.89	18.09	331.39
10541957	4.10	0.61	0.14	0.073	0.291	24.62	2.12	187.82
14367532	4.06	0.52	0.11	0.059	0.351	41.65	9.06	-
37243591	4.00	0.47	0.13	0.054	0.512	52.91	4.64	1673.90
14376612	3.99	0.38	0.12	0.041	0.561	35.74	6.13	169.65
15164105	3.99	0.42	0.25	0.054	0.645	8.19	1.39	141.49
10399889	3.98	0.43	0.15	0.058	0.584	21.74	1.24	563.28
37924223	3.94	0.37	0.16	0.054	0.467	18.07	4.38	73.23
15237073	3.87	0.18	0.09	0.048	0.499	107.22	10.73	257.84
37524376	3.87	0.38	0.09	0.048	0.231	47.36	2.47	-
14444832	3.86	0.28	0.06	0.065	0.315	138.51	7.26	410.03
15503377	3.84	0.25	0.15	0.049	0.149	24.33	1.24	-
37213455	3.81	0.24	0.11	0.052	0.185	66.73	7.60	709.86
11366994	3.80	0.26	0.15	0.053	0.313	21.29	5.14	-
14992276	3.80	0.28	0.09	0.040	0.231	47.12	3.49	-
15538561	3.80	0.23	0.05	0.057	0.356	185.67	20.76	-
37377079	3.46	0.15	0.06	0.049	0.380	82.53	9.83	-

Note. Maximum stress drop estimation exceeds  $10^4$  MPa.

direction. Table 2 documents the inversion results of the 2014  $M_w$  4.58 event using both the single eGf and the weighted stack. The directivity ratio is 0.89 indicating a unilateral rupture. Since we use the weighted stack instead of a single eGf, here we define the residual per degree of freedom as the L2 norm of the differences of the observed and the predicted apparent duration divided by  $m-3$ , where  $m$  is the total number of measurements used for inversion. The residual per degree of freedom is significantly smaller after using the weighted stack in Table 2 indicating an improvement of the data fit.

Similar analyses have been applied to all target earthquakes. The arrows in Figure 10 indicate the centroid rupture velocities in the horizontal and vertical directions. The colors denote the directivity ratios of analyzed target events.

### 3.5. Uncertainty Estimate of Rupture Area and Stress Drop

To estimate stress drops, we follow the approach developed by McGuire and Kaneko (2018) to evaluate the uncertainty in the rupture dimensions. The upper and lower bounds on rupture area (defined as  $\pi \cdot L_c \cdot W_c$ ) permissible for a given data set are determined by convex optimization under the constraint that the data misfit not exceed the 95% confidence interval based on  $\chi^2$  statistics. The  $\chi^2$  statistic is defined as

$$\chi^2 = \sum_i^N \frac{(b_i - \hat{b}_i)^2}{\sigma_i^2} \quad (11)$$

where  $\sigma_i^2$  is the variance of the  $i$ -th measurement. In practice, we assume a constant  $\sigma_i^2$  for all measurements, which is calculated from the minimum residual, for example, the misfit for the optimal second moment estimates  $\sigma^2$ . In addition, we assume  $m-3$  degrees of freedom with  $m$  being the number of measurements used for inversion, so the  $\chi^2$  statistics are  $\chi^2_{95\%,m-3}$ . With this, we can obtain the maximum permissible misfit as  $\sigma^2 \cdot \chi^2_{95\%,m-3}$ , which is used to constrain the misfit level when estimating the maximum/minimum rupture area.

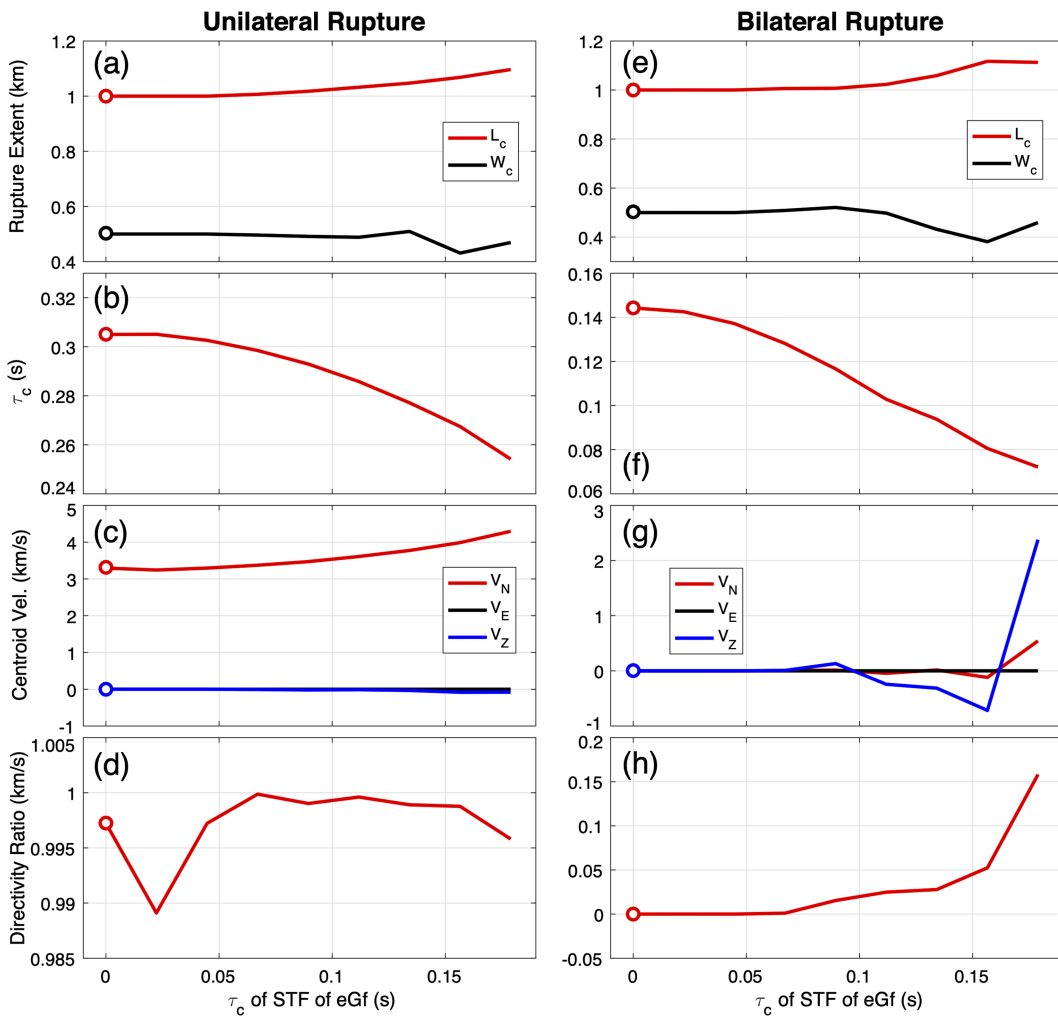


**Figure 9.** Synthetic test results showing the resolution of second moment parameters using synthetic ASTFs deconvolved with eGFs having parabolic STFs of finite duration. The horizontal axis shows the characteristic durations of the parabolic source time functions. Circles in all panels denote the true value of the second moment parameter. The left (a–d) and right (e–h) panels correspond to unilateral and bilateral cases in Figure S7, respectively. (a) Estimated characteristic rupture length  $L_c$  and with  $W_c$ . (b) Estimated characteristic rupture duration  $\tau_c$ . (c) North, east, and vertical components of the resolved centroid rupture velocity. (d) Estimated rupture directivity ratio.

Estimating the maximum rupture area at a particular confidence level can be formulated as:

$$\begin{aligned}
 & \max_{\underline{\underline{\mu}}} \det \underline{\underline{\hat{\mu}}}(2,0) \\
 & \text{subject to } \begin{bmatrix} \underline{\hat{\mu}}^{[0,2]} & \underline{\hat{\mu}}^{[1,1]T} \\ \underline{\hat{\mu}}^{[1,1]} & \underline{\hat{\mu}}^{[2,0]} \end{bmatrix} \geq 0 \\
 & \text{and } \begin{bmatrix} \sigma^2 \cdot \chi^2_{95\%,m-3} & [\underline{b} - \underline{A}\underline{x}]^T \\ \underline{b} - \underline{A}\underline{x} & \underline{\underline{I}}^N \end{bmatrix} \geq 0 \\
 & \text{and } \underline{\hat{\mu}}^{[0,2]} \leq 2 \max[\underline{b}].
 \end{aligned} \tag{12}$$

Solutions of equation (12) set an upper bound on the rupture area  $\pi L_c W_c$ , and hence a lower bound on stress drop. The posed problem is convex and can be solved with convex optimization. However, minimizing  $\det \underline{\underline{\hat{\mu}}}(2,0)$  is not a convex problem. We therefore approximate this problem as

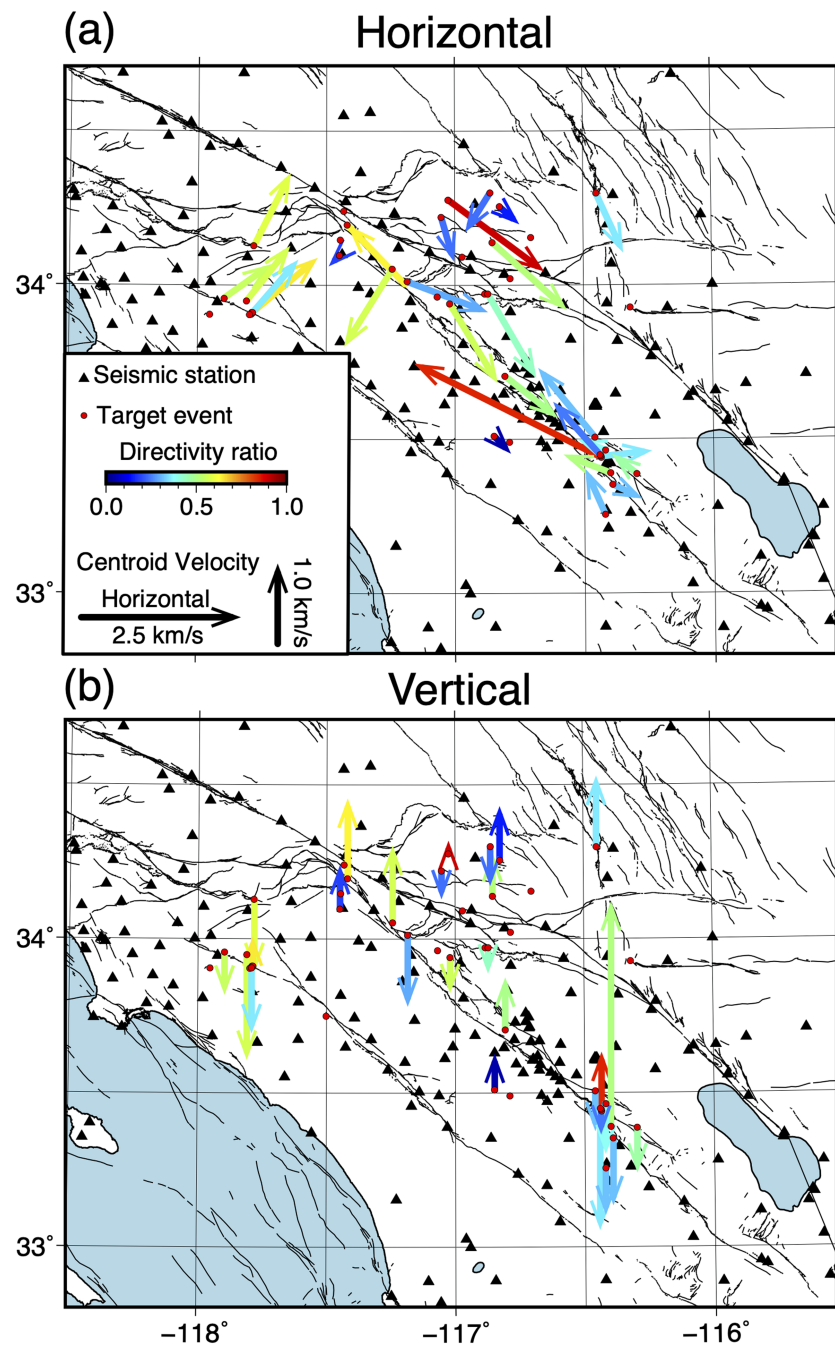


**Figure 10.** Directives in the horizontal (a) and vertical (b) directions of the analyzed target events marked in Figure 1. The arrows show centroid rupture velocities and colors denote directivity ratios.

$$\begin{aligned} & \min L_c^2 + W_c^2 \\ & \text{subject to } \begin{bmatrix} \hat{\mu}^{[0,2]} & \hat{\mu}^{[1,1]T} \\ \hat{\mu}^{[1,1]} & \hat{\mu}^{[2,0]} \end{bmatrix} \geq 0 \\ & \text{and } \begin{bmatrix} \sigma^2 \chi_{95\%, m-3}^2 & [\underline{b} - \underline{A}\underline{x}]^T \\ \underline{b} - \underline{A}\underline{x} & \underline{I}\underline{N} \end{bmatrix} \geq 0 \\ & \text{and } \hat{\mu}^{(0,2)} \leq 2 \max(b). \end{aligned} \quad (13)$$

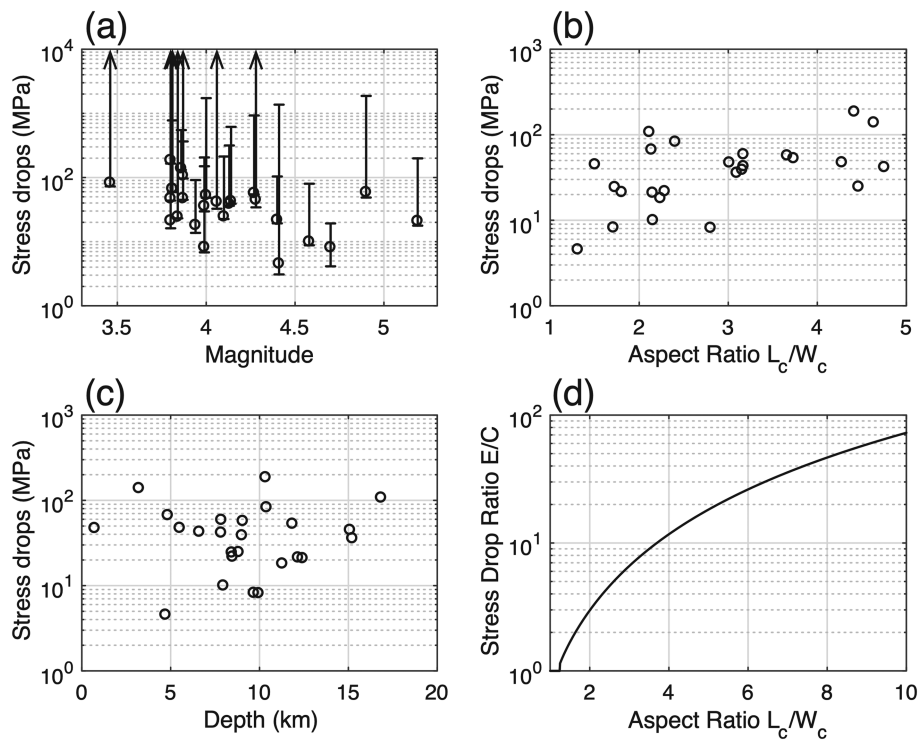


**Figure 11.** (a) Stress drops and uncertainties versus event magnitudes. The vertical arrows indicate the upper bound of stress drops are not well constrained ( $> 10^4$  MPa). (b) Stress drops versus aspect ratio  $L_c/W_c$ . (c) Stress drops versus focal depths. (d) The ratio of stress drops of elliptical/circular cracks with same rupture length. This ratio increases significantly for earthquakes with aspect ratios  $L_c/W_c > 3$ .

Solutions of (13) can roughly estimate the minimum rupture area at a given confidence level (Fan & McGuire, 2018; McGuire & Kaneko, 2018) and give an upper bound on the stress drop.

The rupture is approximated by an ellipse with an area  $S = \pi L_c W_c$  (McGuire & Kaneko, 2018). Assuming the rupture is an elliptical crack in homogeneous elastic medium (Eshelby, 1957), the stress drop is estimated as

$$\Delta\sigma = C(L_c, W_c, \nu) \frac{M_0}{W_c S}, \quad (14)$$

where  $M_0$  is seismic moment and  $C$  is a constant of order unity that depends on the Poisson's ratio  $\nu$  of the medium and aspect ratio of the rupture ellipse. When the aspect ratio  $L_c W_c$  is close to 1 (i.e.,  $< 1.2$ ),  $C(L_c, W_c, \nu)$  is singular, so the stress drop is estimated assuming a circular crack by

$$\Delta\sigma = 2.44 \frac{M_0}{(\pi L_c W_c)^{3/2}}. \quad (15)$$

To estimate stress drops, we first need to convert the magnitudes to seismic moments. For some target events, the magnitudes in the catalog (e.g., Hauksson et al., 2012) are local magnitude  $M_L$ . In such cases, we convert the  $M_L$  values to moment magnitude  $M_w$  using empirical relation documented in the catalog change history of SCSN

$$M_w = 0.853 M_L + 0.40125. \quad (16)$$

Table 3 summarizes stress drop results obtained by our analysis. The optimal stress drop estimates for the 2014  $M_w$  4.58 earthquake is 9.98 MPa and that for the 2013  $M_w$  4.70 earthquake is 8.12 MPa. The corresponding lower and upper bounds are (1.12, 69.99) MPa and (4.00, 11.11) MPa. The excellent station coverage of these two events produces tight bounds on the estimated values. Ross et al. (2017) estimated stress drop

for the 2016  $M_w$  5.19 earthquake using a finite fault model. Their 78.2 MPa stress drop is higher than our optimal estimate 20.9 MPa, but within in the uncertainty range of our 95% confidence level (3.1, 177.9) MPa.

#### 4. Discussion and Conclusions

We describe and implement a semiautomated method employing multiple eGfs for estimating earthquake source properties from second seismic moments. The method includes automated steps of selecting three best performing eGfs using cross correlation and PLD, grid search of stacking weights and finally the second moment inversion. Additional manual corrections are required for some stations (usually a small subset) where the cross correlation may fail to align the waveforms, as the three best performing eGfs can lose some coherency. The duration picks may also need further adjustment after obtaining ASTFs (i.e., Figures 6, 7 and S3–S5) when the ASTF of a station is significantly different from those at nearby stations. The average computing time of the automated steps for one target event on a CPU node with 2 GB memory is ~2 hr. Additional 15 min on average are needed for user involvement to make corrections to the alignments and durations.

This method allows analyzing source properties for a set of earthquakes with little user involvement. Such a technique is necessary for systematic analyses of large data sets. For the southern California data set used in this paper, we perform second moment analyses using weighted stacked eGfs for target events with measurements of ASTFs accepted at 15 or more stations that provide good azimuthal coverage. The horizontal component of the rupture directivities is usually well constrained with good azimuthal coverage for strike slip events (e.g., Figures 8c and 8f). The along-dip component of the rupture directivity can only be well constrained when stations are available directly above the hypocenter because the seismic rays take off almost horizontally for most other stations. For events with less good station coverage (less than 15 measurements), we relax our criteria for stations in the azimuthal gaps or right above the hypocenter (i.e., accepting measurements with normalized misfit <0.35 instead of 0.3).

A detailed comparison of results of the 2014  $M_w$  4.58 event using single eGf and stacked eGf is documented in Table 2. For this event, the weighted stack results in 10 more stations with accepted measurements and smaller residuals per degree of freedom, which improves the station coverage and data fit. Table 3 shows the second moment inversion results for the analyzed target events with magnitudes  $M$  3.5 and above. Smaller events ( $M < 3.5$ ) are not resolvable because the SNR of eGfs are too low to get stable ASTF estimates in the PLD. The results in Table 3 show that target events with larger magnitudes generally result in larger estimates of  $L_c$  and  $\tau_c$  as expected (Figures S6a and S6b). A similar but weaker trend of the magnitude and rupture directivity ratio (Figure S6c) may indicate that large earthquakes are more likely to develop strong rupture directivities in the study area because of the larger rupture area and longer rupture time.

The estimated  $\tau_c$  for the target events can be slightly underestimated because the STFs of the eGfs are not an ideal Dirac delta function. To evaluate this effect on the estimated  $\tau_c$ ,  $L_c$ , centroid velocity, and directivity ratio, we perform synthetic tests with two representative rupture models. Each model has an elliptical rupture area striking north and dipping vertically with a hypocenter at 10 km depth. Figures S7a and S7b show the rupture times for a unilateral rupture initiated from the southernmost edge of the ellipse, and for a bilateral rupture initiated at the center, respectively. The rupture propagation velocity is fixed at 3.2 km/s, which is smaller than the average  $S$  wave velocity at this depth based on a 1-D velocity model averaged from the community velocity model for Southern California (CVM-S4.26; Lee et al., 2014). We discretize the elliptical rupture area into  $2\text{ m} \times 2\text{ m}$  cells and assume a uniform slip with a rake angle of  $0^\circ$ . The slip rate for each cell is a parabolic function with a rise time of 0.1 s. We randomly generate 30 stations on top of the source within an epicentral distance of 120 km. Figures S7c and S7d show the azimuthal and take-off angle coverage of the stations. To guarantee good coverage, there are both up-going (take-off angle  $>90^\circ$ ) and down-going rays (take-off angle  $<90^\circ$ ) and no significant azimuthal gaps ( $>45^\circ$ ). We then synthesize the ASTF and corresponding apparent  $\tau_c(S)$  of the  $S$  phase at each station for both models. The colored circles in Figures S7c and S7d present the apparent  $\tau_c$  of the noise free synthetic ASTFs. The estimated  $L_c$ ,  $\tau_c$ , centroid velocity, and directivity ratio for the two models using equations (6)–(10) are shown as the circles in Figure 9. These resolved second moments are identical to the results computed using equations (2)–(5).

A realistic estimated ASTF of the target earthquake is the deconvolution of the true ASTF of the target earthquake by the ASTF of the eGf. As the rupture duration of the eGf is significantly smaller than the target earthquake, the ASTF of eGf can be approximated by a uniform STF (e.g., a parabolic pulse) in all directions. To evaluate the effect of deconvolving realistic eGfs from the records, we deconvolve all the synthetic ASTFs by a parabolic STF with a finite duration. By measuring the characteristic durations of the deconvolved ASTFs and performing the second moment inversion, we estimate the finite source parameters shown in Figure 9 with different durations of the STFs of the eGf. The characteristic rupture durations for both the unilateral and bilateral rupture models are slightly underestimated, while the variations of the characteristic rupture length  $L_c$  and width  $W_c$  are negligible when the characteristic duration of the eGf ( $\tau_c^{\text{eGf}}$ ) is smaller than a third of the target event ( $\tau_c^{\text{tar}}$ ). The centroid rupture velocity is therefore slightly overestimated for the unilateral rupture model. The directivity ratios for both models and the centroid rupture velocity of the bilateral rupture model remain almost unchanged when  $\tau_c^{\text{eGf}} < \frac{1}{3} \tau_c^{\text{tar}}$ . This indicates that the estimates using the second moment method with a good station coverage are stable. In applications, an eGf can be consider a point source when its rupture length and duration is significantly shorter (e.g., 5 times less) than the target event. The rupture duration  $\tau_c$  and seismic moment  $M_0$  generally follow to the first order the cube-root scaling law  $\tau_c \sim M_0^{1/3}$  (e.g., Kanamori & Anderson, 1975; Ekström & Engdahl, 1989; Houston, 2001). Therefore, considering the moment magnitude scale, the rupture duration  $\tau_c$  and the moment magnitude  $M_w$  follow  $\tau_c \sim 10^{4M_w}$  (Hanks & Kanamori, 1979; Kanamori, 1977). The eGf then should be 1.4 magnitude units less than the event of interest.

The centroid directivities of all target events (Figure 10) are consistent with the independent results of Kurzon et al. (2014) and Ross and Ben-Zion (2016) based on ratios of ground motion and source spectra in different directions. Most events in the central San Jacinto fault zone have directivities to the northwest, while most events around Cajon Pass and San Gabriel Mountain have directivities to the southeast. The observations imply that the ruptures tend to propagate in the direction of motion of slow sides of the imaged velocity contrasts (e.g., Allam & Ben-Zion, 2012; Zigone et al., 2015; Share & Ben-Zion, 2018; Share, Allam, et al., 2019). These results are generally consistent with expectations for dynamic rupture on a bimaterial interface (e.g., Ampuero & Ben-Zion, 2008; Andrews & Ben-Zion, 1997; Ben-Zion, 2001; Brietzke & Ben-Zion, 2006; Ranjith & Rice, 2001; Shlomai & Fineberg, 2016; Weertman, 1980). A few events show directivities in near-normal direction to the major fault. This is consistent with observed lineations of seismicity, surface fault traces and velocity structures normal to the main faults (e.g., Ross et al., 2017; Share, Guo, et al., 2019). Applying our method to other areas with large strike slip faults such as Turkey, Israel, New Zealand, and Indonesia will further enlarge the data set of observations and help to test how bimaterial interfaces affect rupture directivities.

The stress drops and corresponding upper and lower bounds of the target events are estimated by the approach developed by McGuire and Kaneko (2018). Table 3 and Figure 11 show that the results span a range of 2–145 MPa. The lower bounds of the stress drop, corresponding to maximum rupture area, are always well constrained. The upper bounds of a considerable number of events can exceed  $10^4$  MPa, indicating they are not well constrained. This asymmetry results from the difficulty in rejecting excessively small rupture widths for some station geometries, typically relatively shallow events that lack multiple observations of upgoing phases. The stress drop estimates are also sensitive to focal depth, which affects the take-off angles connecting the source and stations. The rupture area estimates are well constrained if the events have both up-going and down-going rays.

We assume that the crack model applies for stress drop estimates (equation (14)), as in the methods that use corner frequency measurements (e.g., Brune, 1970; Madariaga, 1976). However, instead of assuming a circular crack we estimate both the major and minor axes of an elliptical rupture area ( $L_c$  and  $W_c$ ). Figure 11b shows a correlation between the stress drop estimates and aspect ratio estimates  $L_c/W_c$ , as expected from the term  $C(L_c, W_c, \nu)$  in equation (14). However, the factor of  $\sim 5$  variability around this trend indicates that natural variability in the ratio of rupture length to moment remains important even after accounting for aspect ratio. Figure 11d shows ratios of stress drop estimates of elliptical and circular cracks with the same rupture length  $L_c$  but different rupture width  $W_c$ . The stress drops of the elliptical crack are significantly higher when the aspect ratio is  $\geq 3$ . This suggests that stress drops are likely to be systematically underestimated by methods that assume a circular crack model (e.g., the corner frequency method) that only

constrains one rupture dimension. Our results indicate that many events have aspect ratios in the 2–5 range. If this holds in larger data sets, it would imply that many previous studies assuming circular cracks systematically underestimate stress drops by a factor of ~5–10.

In this paper, we have focused on developing a semiautomated technique for estimating a variety of different source properties with little user involvement (Figure 2). The developed approach stably resolves the finite source properties of small to moderate earthquakes and can be used to perform systematic analysis of large data sets. Our results on the rupture directivity are consistent with expectations associated with ruptures on bimaterial interfaces in southern California. The existence of statistically persistent earthquake directivities on given fault sections is important for seismic hazard analysis in terms of estimating ground motion from large earthquake on major faults. Applying our method to data sets with different tectonic settings, such as in northern California, Japan, and southwest China, will allow testing further the generality of the obtained results and examine if source properties vary between different regions.

## Acknowledgments

The seismic data used in this study were obtained from the Southern California Earthquake Data Center (*SCEDC*, 2013; <http://scedc.caltech.edu/>). The study was supported by the Southern California Earthquake Center (based on NSF Cooperative Agreement EAR-1600087 and U.S. Geological Survey Cooperative Agreement G17AC00047) and the US-Israel Bi-national Science Foundation (BSF Grant 2016043). The paper benefitted from useful comments by Thomas Hanks, Elizabeth Cochran, Naofumi Aso, an anonymous referee, and an anonymous Associate Editor.

## References

- Abercrombie, R. E. (2015). Investigating uncertainties in empirical Green's function analysis of earthquake source parameters. *Journal of Geophysical Research: Solid Earth*, 120, 4263–4277. <https://doi.org/10.1002/2015JB011984>
- Allam, A. A., & Ben-Zion, Y. (2012). Seismic velocity structures in the Southern California plate-boundary environment from double-difference tomography. *Geophysical Journal International*, 190(2), 1181–1196. <https://doi.org/10.1111/j.1365-246X.2012.05544.x>
- Ampuero, J. P., & Ben-Zion, Y. (2008). Cracks, pulses and macroscopic asymmetry of dynamic rupture on a bimaterial interface with velocity-weakening friction. *Geophysical Journal International*, 173(2), 674–692. <https://doi.org/10.1111/j.1365-246X.2008.03736.x>
- Andrews, D. J., & Ben-Zion, Y. (1997). Wrinkle-like slip pulse on a fault between different materials. *Journal of Geophysical Research*, 102(B1), 553–571. <https://doi.org/10.1029/96JB02856>
- Andrews, D. J., & Harris, R. A. (2005). The wrinkle-like slip pulse is not important in earthquake dynamics. *Geophysical Research Letters*, 32, L23303. <https://doi.org/10.1029/2005gl023996>
- Backus, G., & Mulcahy, M. (1976a). Moment tensors and other phenomenological descriptions of seismic sources—I. Continuous displacements. *Geophysical Journal International*, 46(2), 341–361. <https://doi.org/10.1111/j.1365-246X.1976.tb04162.x>
- Backus, G., & Mulcahy, M. (1976b). Moment tensors and other phenomenological descriptions of seismic sources—II. Discontinuous displacements. *Geophysical Journal International*, 47(2), 301–329. <https://doi.org/10.1111/j.1365-246X.1976.tb01275.x>
- Backus, G. E. (1977a). Interpreting the seismic glut moments of total degree two or less. *Geophysical Journal International*, 51(1), 1–25. <https://doi.org/10.1111/j.1365-246X.1977.tb04187.x>
- Backus, G. E. (1977b). Seismic sources with observable glut moments of spatial degree two. *Geophysical Journal International*, 51(1), 27–45. <https://doi.org/10.1111/j.1365-246X.1977.tb04188.x>
- Baltay, A., Prieto, G., & Beroza, G. C. (2010). Radiated seismic energy from coda measurements and no scaling in apparent stress with seismic moment. *Journal of Geophysical Research*, 115, B08314. <https://doi.org/10.1029/2009JB006736>
- Ben-Zion, Y. (2001). Dynamic ruptures in recent models of earthquake faults. *Journal of the Mechanics and Physics of Solids*, 49(9), 2209–2244. [https://doi.org/10.1016/S0022-5096\(01\)00036-9](https://doi.org/10.1016/S0022-5096(01)00036-9)
- Ben-Zion, Y., & Huang, Y. (2002). Dynamic rupture on an interface between a compliant fault zone layer and a stiffer surrounding solid. *Journal of Geophysical Research*, 107(B2), 2042. <https://doi.org/10.1029/2001JB000254>
- Ben-Zion, Y., & Zhu, L. (2002). Potency-magnitude scaling relations for southern California earthquakes with  $1.0 < M_L < 7.0$ . *Geophysical Journal International*, 148(3), F1–F5. <https://doi.org/10.1046/j.1365-246X.2002.01637.x>
- Bertero, M., Bindu, D., Boccacci, P., Cattaneo, M., Eva, C., & Lanza, V. (1997). Application of the projected Landweber method to the estimation of the source time function in seismology. *Inverse Problems*, 13(2), 465.
- Boyd, S., & Vandenberghe, L. (2004). *Convex optimization*. Cambridge University Press. <https://doi.org/10.1017/CBO9780511804441>
- Brietzke, G. B., & Ben-Zion, Y. (2006). Examining tendencies of in-plane rupture to migrate to material interfaces. *Geophysical Journal International*, 167, 807–819. <https://doi.org/10.1111/j.1365-246X.2006.03137.x>
- Brietzke, G. B., Cochard, A., & Igel, H. (2009). Importance of bimaterial interfaces for earthquake dynamics and strong ground motion. *Geophysical Journal International*, 178(2), 921–938. <https://doi.org/10.1111/j.1365-246X.2009.04209.x>
- Brune, J. N. (1970). Tectonic stress and the spectra of seismic shear waves from earthquakes. *Journal of Geophysical Research*, 75(26), 4997–5009. <https://doi.org/10.1029/JB075i026p04997>
- Calderoni, G., Rovelli, A., Ben-Zion, Y., & Di Giovambattista, R. (2015). Along-strike rupture directivity of earthquakes of the 2009 L'Aquila, central Italy, seismic sequence. *Geophysical Journal International*, 203(1), 399–415. <https://doi.org/10.1093/gji/ggv275>
- Calderoni, G., Rovelli, A., & Singh, S. K. (2012). Stress drop and source scaling of the 2009 April L'Aquila earthquakes. *Geophysical Journal International*, 192(1), 260–274. <https://doi.org/10.1093/gji/ggs011>
- Di Bartolomeo, M., Meziane, A., Massi, F., Baillet, L., & Fregolent, A. (2010). Dynamic rupture at a frictional interface between dissimilar materials with asperities. *Tribology International*, 43(9), 1620–1630.
- Dor, O., Rockwell, T. K., & Ben-Zion, Y. (2006). Geological observations of damage asymmetry in the structure of the San Jacinto, San Andreas and Punchbowl faults in Southern California: A possible indicator for preferred rupture propagation direction. *Pure and Applied Geophysics*, 163(2–3), 301–349. <https://doi.org/10.1007/s00024-005-0023-9>
- Dor, O., Yildirim, C., Rockwell, T. K., Ben-Zion, Y., Emre, O., Sisk, M., & Duman, T. Y. (2008). Geologic and geomorphologic asymmetry across the rupture zones of the 1943 and 1944 earthquakes on the North Anatolian Fault: Possible signals for preferred earthquake propagation direction. *Geophysical Journal International*, 173, 483–504. <https://doi.org/10.1111/j.1365-246X.2008.03709.x>
- Eberhart-Phillips, D., & Michael, A. J. (1993). Three-dimensional velocity structure, seismicity, and fault structure in the Parkfield region, central California. *Journal of Geophysical Research*, 98(B9), 15,737–15,758.
- Ekström, G., & Engdahl, E. R. (1989). Earthquake source parameters and stress distribution in the Adak Island region of the central Aleutian Islands, Alaska. *Journal of Geophysical Research*, 94(B11), 15,499–15,519.

- Erickson, B. A., & Day, S. M. (2016). Bimaterial effects in an earthquake cycle model using rate-and-state friction. *Journal of Geophysical Research: Solid Earth*, 121, 2480–2506.
- Eshelby, J. D. (1957). The determination of the elastic field of an ellipsoidal inclusion, and related problems. *Proceedings of the Royal Society of London. Series A. Mathematical and Physical Sciences*, 241(1226), 376–396. <https://doi.org/10.1098/rspa.1957.0133>
- Fan, W., & McGuire, J. J. (2018). Investigating microearthquake finite source attributes with IRIS Community Wavefield Demonstration Experiment in Oklahoma. *Geophysical Journal International*, 214(2), 1072–1087. <https://doi.org/10.1093/gji/ggy203>
- Goebel, T., Hauksson, E., Shearer, P., & Ampuero, J. (2015). Stress-drop heterogeneity within tectonically complex regions: A case study of San Gorgonio Pass, southern California. *Geophysical Journal International*, 202(1), 514–528.
- Grant, M., & Boyd, S. (2014). CVX: Matlab software for disciplined convex programming, version 2.1.
- Grant, M. C., & Boyd, S. P. (2008). *Graph implementations for nonsmooth convex programs*, In: *Recent advances in learning and control* (pp. 95–110). London: Springer. [https://doi.org/10.1007/978-1-84800-155-8\\_7](https://doi.org/10.1007/978-1-84800-155-8_7)
- Hanks, T. C., & Kanamori, H. (1979). A moment magnitude scale. *Journal of Geophysical Research*, 84(B5), 2348–2350.
- Harris, R., & Day, S. (2005). Material contrast does not predict earthquake rupture propagation direction. *Geophysical Research Letters*, 32, L23301. <https://doi.org/10.1029/2005GL023941>
- Harris, R. A., & Day, S. M. (1997). Effects of a low-velocity zone on a dynamic rupture. *Bulletin of the Seismological Society of America*, 87(5), 1267–1280.
- Hart, E. W., Bryant, W. A., Wills, C. J., Treiman, J. A., & Kahle, J. E. (1989). Summary Report: Fault evaluation program, 1987–1988, southwestern basin and range region and supplemental areas. *Department of Conservation, Division of Mines and Geology Open-File Report*, 89–16.
- Hartzell, S. H. (1978). Earthquake aftershocks as Green's functions. *Geophysical Research Letters*, 5(1), 1–4.
- Hauksson, E., Yang, W., & Shearer, P. M. (2012). Waveform relocated earthquake catalog for southern California (1981 to June 2011). *Bulletin of the Seismological Society of America*, 102(5), 2239–2244. <https://doi.org/10.1785/0120120010>
- Hillers, G., Ben-Zion, Y., Landes, M., & Campillo, M. (2013). Interaction of microseisms with crustal heterogeneity: A case study from the San Jacinto fault zone area. *Geochemistry, Geophysics, Geosystems*, 14(7), 2182–2197. <https://doi.org/10.1002/ggge.20140>
- Hough, S. E., & Dreger, D. S. (1995). Source parameters of the 23 April 1992 M 6.1 Joshua Tree, California, earthquake and its aftershocks: Empirical Green's function analysis of GEOS and TERRAscope data. *Bulletin of the Seismological Society of America*, 85(6), 1576–1590.
- Houston, H. (2001). Influence of depth, focal mechanism, and tectonic setting on the shape and duration of earthquake source time functions. *Journal of Geophysical Research*, 106(B6), 11,137–11,150.
- Houston, H., & Kanamori, H. (1986). Source spectra of great earthquakes: Teleseismic constraints on rupture process and strong motion. *Bulletin of the Seismological Society of America*, 76(1), 19–42.
- Hutchings, L., & Wu, F. (1990). Empirical Green's functions from small earthquakes: A waveform study of locally recorded aftershocks of the 1971 San Fernando earthquake. *Journal of Geophysical Research*, 95(B2), 1187–1214. <https://doi.org/10.1029/JB095iB02p01187>
- Inbal, A., Cristea-Platon, T., Ampuero, J. P., Hillers, G., Agnew, D., & Hough, S. E. (2018). Sources of long-range anthropogenic noise in Southern California and implications for tectonic tremor detection. *Bulletin of the Seismological Society of America*, 108(6), 3511–3527. <https://doi.org/10.1785/0120180130>
- Johnson, C. W., Meng, H., Vernon, F., & Ben-Zion, Y. (2019). Characteristics of ground motion generated by wind interaction with trees, structures, and other surface obstacles. *Journal of Geophysical Research: Solid Earth*. <https://doi.org/10.1029/2018JB017151>
- Kanamori, H. (1977). The energy release in great earthquakes. *Journal of Geophysical Research*, 82(20), 2981–2987.
- Kanamori, H., & Anderson, D. L. (1975). Theoretical basis of some empirical relations in seismology. *Bulletin of the Seismological Society of America*, 65(5), 1073–1095.
- Kane, D. L., Shearer, P. M., Goertz-Allmann, B. P., & Vernon, F. L. (2013). Rupture directivity of small earthquakes at Parkfield. *Journal of Geophysical Research: Solid Earth*, 118. <https://doi.org/10.1029/2012JB009675>
- Kurzon, I., Vernon, F. L., Ben-Zion, Y., & Atkinson, G. (2014). Ground motion prediction equations in the San Jacinto fault zone: Significant effects of rupture directivity and fault zone amplification. *Pure and Applied Geophysics*, 171(11), 3045–3081.
- Lanza, V., Spallarossa, D., Cattaneo, M., Bindi, D., & Augliera, P. (1999). Source parameters of small events using constrained deconvolution with empirical Green's functions. *Geophysical Journal International*, 137(3), 651–662. <https://doi.org/10.1046/j.1365-246x.1999.00809.x>
- Lee, E. J., Chen, P., Jordan, T. H., Maechling, P. B., Denolle, M. A., & Beroza, G. C. (2014). Full-3-D tomography for crustal structure in southern California based on the scattering-integral and the adjoint-wavefield methods. *Journal of Geophysical Research: Solid Earth*, 119, 6421–6451. <https://doi.org/10.1002/2014JB011346>
- Lengliné, O., & Ampuero, J.-P. (2015). Insights on earthquake triggering processes from early aftershocks of repeating microearthquakes. *Journal of Geophysical Research: Solid Earth*, 120, 6977–6992. <https://doi.org/10.1002/2015JB012287>
- Lengliné, O., & Got, J. L. (2011). Rupture directivity of microearthquake sequences near Parkfield, California. *Geophysical Research Letters*, 38. <https://doi.org/10.1029/2011GL047303>
- Lewis, M. A., Peng, Z., Ben-Zion, Y., & Vernon, F. L. (2005). Shallow seismic trapping structure in the San Jacinto fault zone near Anza, California. *Geophysical Journal International*, 162(3), 867–881.
- Li, Z., & Peng, Z. (2016). An automatic phase picker for local earthquakes with predetermined locations: Combining a signal-to-noise ratio detector with 1D velocity model inversion. *Seismological Research Letters*, 87(6), 1397–1405. <https://doi.org/10.1785/0220160027>
- Madariaga, R. (1976). Dynamics of an expanding circular fault. *Bulletin of the Seismological Society of America*, 66(3), 639–666.
- McGuire, J. J. (2004). Estimating finite source properties of small earthquake ruptures. *Bulletin of the Seismological Society of America*, 94(2), 377–393. <https://doi.org/10.1785/0120030091>
- McGuire, J. J. (2017). A MATLAB toolbox for estimating the second moments of earthquake ruptures. *Seismological Research Letters*, 88(2A), 371–378. <https://doi.org/10.1785/0220160170>
- McGuire, J. J., & Kaneko, Y. (2018). Directly estimating earthquake rupture area using second moments to reduce the uncertainty in stress drop. *Geophysical Journal International*, 214(3), 2224–2235. <https://doi.org/10.1093/gji/ggy201>
- McGuire, J. J., Zhao, L., & Jordan, T. H. (2001). Teleseismic inversion for the second degree moments of earthquake space-time distributions. *Geophysical Journal International*, 145(3), 661–678. <https://doi.org/10.1046/j.1365-246x.2001.01414.x>
- Meng, H., & Ben-Zion, Y. (2018). Characteristics of airplanes and helicopters recorded by a dense seismic array near Anza California. *Journal of Geophysical Research: Solid Earth*, 123, 4783–4797. <https://doi.org/10.1029/2017JB015240>
- Mitchell, T. M., Ben-Zion, Y., & Shimamoto, T. (2011). Pulverized fault rocks and damage asymmetry along the Arima-Takatsuki Tectonic Line, Japan. *Earth and Planetary Science Letters*, 308(3–4), 284–297.

- Mueller, C. S. (1985). Source pulse enhancement by deconvolution of an empirical Green's function. *Geophysical Research Letters*, 12(1), 33–36. <https://doi.org/10.1029/GL012i001p00033>
- Prieto, G. A., Shearer, P. M., Vernon, F. L., & Kilb, D. (2004). Earthquake source scaling and self-similarity estimation from stacking *P* and *S* spectra. *Journal of Geophysical Research*, 109, B08310. <https://doi.org/10.1029/2004jb003084>
- Ranjith, K., & Rice, J. R. (2001). Slip dynamics at an interface between dissimilar materials. *Journal of the Mechanics and Physics of Solids*, 49(2), 341–361. [https://doi.org/10.1016/S0022-5096\(00\)00029-6](https://doi.org/10.1016/S0022-5096(00)00029-6)
- Ross, Z. E., & Ben-Zion, Y. (2013). Spatio-temporal variations of double-couple aftershock mechanisms and possible volumetric earthquake strain. *Journal of Geophysical Research: Solid Earth*, 118, 2347–2355. <https://doi.org/10.1002/jgrb.50202>
- Ross, Z. E., & Ben-Zion, Y. (2016). Toward reliable automated estimates of earthquake source properties from body wave spectra. *Journal of Geophysical Research: Solid Earth*, 121, 4390–4407. <https://doi.org/10.1002/2016JB013003>
- Ross, Z. E., Hauksson, E., & Ben-Zion, Y. (2017). Abundant off-fault seismicity and orthogonal structures in the San Jacinto fault zone. *Science Advances*, 3(3), e1601946. <https://doi.org/10.1126/sciadv.1601946>
- Rubin, A. M., & Gillard, D. (2000). Aftershock asymmetry/rupture directivity among central San Andreas fault microearthquakes. *Journal of Geophysical Research*, 105(B8), 19,095–19,109. <https://doi.org/10.1029/2000JB900129>
- Share, P. E., Allam, A. A., Ben-Zion, Y., Lin, F. C., & Vernon, F. L. (2019). Structural properties of the San Jacinto fault zone at Blackburn Saddle from seismic data of a dense linear array. *Pure and Applied Geophysics*, 176(3), 1169–1191. <https://doi.org/10.1007/s00024-018-1988-5>
- Share, P. E., & Ben-Zion, Y. (2018). A bimaterial interface along the northern San Jacinto Fault through Cajon Pass. *Geophysical Research Letters*, 45(21), 11–622. <https://doi.org/10.1029/2018GL079834>
- Share, P. E., Guo, H., Thurber, C. H., Zhang, H., & Ben-Zion, Y. (2019). Seismic imaging of the southern California plate boundary around the south-central transverse ranges using double-difference tomography. *Pure and Applied Geophysics*, 176(3), 1117–1143. <https://doi.org/10.1007/s00024-018-2042-3>
- Shearer, P. M., Prieto, G. A., & Hauksson, E. (2006). Comprehensive analysis of earthquake source spectra in southern California. *Journal of Geophysical Research Solid Earth*, 111, B06303. <https://doi.org/10.1029/2005JB003979>
- Shi, Z., & Ben-Zion, Y. (2006). Dynamic rupture on a bimaterial interface governed by slip-weakening friction. *Geophysical Journal International*, 165(2), 469–484. <https://doi.org/10.1111/j.1365-246X.2006.02853.x>
- Shlomai, H., & Fineberg, J. (2016). The structure of slip-pulses and supershear ruptures driving slip in bimaterial friction. *Nature Communications*, 7, 11787. <https://doi.org/10.1038/ncomms11787>
- Southern California Earthquake Data Center (SCEDC) (2013). Southern California Earthquake Center, dataset. *California Institute of Technology*. <https://doi.org/10.7909/C3WD3xH1>
- Thurber, C., Zhang, H., Waldhauser, F., Hardebeck, J., Michael, A., & Eberhart-Phillips, D. (2006). Three-dimensional compressional wavespeed model, earthquake relocations, and focal mechanisms for the Parkfield, California, region. *Bulletin of the Seismological Society of America*, 96(4B), S38–S49.
- Uchide, T., Shearer, P. M., & Imanishi, K. (2014). Stress drop variations among small earthquakes before the 2011 Tohoku-oki, Japan, earthquake and implications for the main shock. *Journal of Geophysical Research: Solid Earth*, 119, 7164–7174.
- Vandenberghe, L., & Boyd, S. (1996). Semidefinite programming. *SIAM Review*, 38(1), 49–95. <https://doi.org/10.1137/1038003>
- Vernon, F. L. (1982). ANZA regional network. *International Federation of Digital Seismograph Networks. Dataset/Seismic Network*. <https://doi.org/10.7914/SN/AZ>
- Wang, E., & Rubin, A. M. (2011). Rupture directivity of microearthquakes on the San Andreas Fault from spectral ratio inversion. *Geophysical Journal International*, 186(2), 852–866. <https://doi.org/10.1111/j.1365-246X.2011.05087.x>
- Wang, E., Rubin, A. M., & Ampuero, J. P. (2014). Compound earthquakes on a bimaterial interface and implications for rupture mechanics. *Geophysical Journal International*, 197(2), 1138–1153.
- Weertman, J. (1980). Unstable slippage across a fault that separates elastic media of different elastic constants. *Journal of Geophysical Research*, 85(B3), 1455–1461. <https://doi.org/10.1029/JB085iB03p01455>
- White, M. C., Ben-Zion, Y., & Vernon, F. L. (2019). A detailed earthquake catalog for the San Jacinto fault-zone region in southern California. *Journal of Geophysical Research: Solid Earth*, 124, 6908–6930. <https://doi.org/10.1029/2019JB017641>
- Yang, W., & Ben-Zion, Y. (2010). An algorithm for detecting clipped waveforms and suggested correction procedures. *Seismological Research Letters*, 81(1), 53–62. <https://doi.org/10.1785/gssrl.81.1.53>
- Yang, W., Hauksson, E., & Shearer, P. M. (2012). Computing a large refined catalog of focal mechanisms for southern California (1981–2010): Temporal stability of the style of faulting. *Bulletin of the Seismological Society of America*, 102(3), 1179–1194. <https://doi.org/10.1785/0120110311>
- Zaliapin, I., & Ben-Zion, Y. (2011). Asymmetric distribution of aftershocks on large faults in California. *Geophysical Journal International*, 185(3), 1288–1304. <https://doi.org/10.1111/j.1365-246X.2011.04995.x>
- Zhao, L. S., & Helmberger, D. V. (1994). Source estimation from broadband regional seismograms. *Bulletin of the Seismological Society of America*, 84(1), 91–104.
- Zhu, L., & Ben-Zion, Y. (2013). Parameterization of general seismic potency and moment tensors for source inversion of seismic waveform data. *Geophysical Journal International*, 194, 839–843. <https://doi.org/10.1093/gji/ggt137>
- Zhu, L., & Helmberger, D. V. (1996). Advancement in source estimation techniques using broadband regional seismograms. *Bulletin of the Seismological Society of America*, 86(5), 1634–1641.
- Zigone, D., Ben-Zion, Y., Campillo, M., & Roux, P. (2015). Seismic tomography of the Southern California plate boundary region from noise-based Rayleigh and Love waves. *Pure and Applied Geophysics*, 172(5), 1007–1032. <https://doi.org/10.1007/s00024-014-0872-1>